OPEN ACCESS
Journal of Innovative Optical Health Sciences
Vol. 17, No. 1 (2024) 2330008 (27 pages)

DOI: 10.1142/S1793545823300082

World Scientific
www.worldscientific.com

Laser spectroscopy imaging technique coupled with nanomaterials for cancer diagnosis: A review

Zhengying Peng*, Pengkun Yin‡, Dan Li§, Youyuan Chen*, Kaiqiang Shu†, Qingwen Fan†, Yixiang Duan† and Qingyu Lin†,¶

*Key Laboratory of Bio-Resource and Eco-Environment
Ministry of Education, College of Life Sciences
Sichuan University Chengdu 610064
Sichuan, P. R. China

†Research Center of Analytical Instrumentation
School of Mechanical Engineering
Sichuan University, Chengdu 610064, Sichuan, P. R. China

‡Key Laboratory of Green Chemistry & Technology of Ministry of Education
College of Chemistry, Sichuan University Chengdu 610064
Sichuan, P. R. China

§State Key Laboratory of Membrane Biology
Beijing Advanced Innovation Center for Structural Biology
School of Life Sciences
Tsinghua University, Beijing 100084, P. R. China
¶qylin@scu.edu.cn

Received 27 January 2023
Revised 15 March 2023
Accepted 15 March 2023
Published 19 May 2023

Laser spectroscopic imaging techniques have received tremendous attention in the field of cancer diagnosis due to their high sensitivity, high temporal resolution, and short acquisition time. However, the limited tissue penetration of the laser is still a challenge for the *in vivo* diagnosis of deep-seated lesions. Nanomaterials have been universally integrated with spectroscopic imaging techniques for deeper cancer diagnosis *in vivo*. The components, morphology, and sizes of nanomaterials are delicately designed, which could realize cancer diagnosis *in vivo* or *in situ*. Considering the enhanced signal emitting from the nanomaterials, we emphasized their combination with spectroscopic imaging techniques for cancer diagnosis, like the surface-enhanced Raman scattering (SERS), photoacoustic, fluorescence, and laser-induced breakdown spectroscopy (LIBS). Applications of the above spectroscopic techniques offer new prospects for cancer diagnosis.

Keywords: Laser spectroscopy; tumor imaging; tumor diagnosis; nanomaterials.

1. Introduction

In 2020, 10.0 million cancer deaths and 19.3 million new cancer cases have occurred,[1] which has become a dominant cause of death and a barrier to every country of the world for a long time. Not only the diagnosis of cancer but also prevention of misdiagnosis and overdiagnosis are vitally important as better follow-up therapy. Therefore, it's crucial to diagnose the tumor region before, during and after surgery. Traditional imaging methods for tumor diagnosis have been universally used in current clinical diagnosis (Doppler imaging, computed tomography, positron emission tomography, and magnetic resonance imaging listed in Table S1, abbreviation: CT, PET, and MRI).[2] Although these techniques are well-established, there are still limitations in terms of patient testing and diagnostic specificity and sensitivity. For example, people who implanted metal devices can't be scanned by MRI[3]; radiation from CT and PET is a burden for tumor patients.[4] Additionally, the biopsy guidance of MRI and PEI during surgery is limited due to the magnetic fields and radioactive environment, which is not suitable for real-time and *in situ* imaging.[5] To provide adequate tumor diagnosis, spectroscopic techniques can be used as a complementary technique to traditional techniques.

Laser spectroscopic techniques, based on the interaction between photons and the substance, generate innumerous optical processes.[6–10] It is mainly the collection of different excited lights that distinguishes the various techniques. For example, collection of scattered light is Raman technique, collection of light from energy state transitions is fluorescent, collection of acoustics into optics is photoacoustic, collection of light emitted from plasma is laser-induced breakdown spectroscopy (LIBS), etc. In short, the different forms of light emitted after excitation of the laser beam differentiate the spectroscopic techniques separately. Laser spectroscopic imaging is performed by scanning an array of tissue sites. The spectral information from each point is stitched together to create a map of the entire tissue. Therefore, diagnosis of tumor areas is assisted by the spectral differences between normal and tumor tissues. Thus, the label-free diagnosis method is achieved. The tumor diagnosis of spectroscopic techniques could be achieved *in vivo* and *in situ*, but also *ex vitro* biopsy. However, the existence of tumor heterogeneity will make each individual tumor different. It is also difficult to make accurate judgment by the spectral information from substances, which requires for harsh software and hardware. To improve the imaging depth, accuracy and specificity, spectroscopic techniques coupled with nanomaterials for tumor diagnosis have been studied.

The nanotechnology has made tremendous advances in recent years, which could actively target specific sites or be remained passively through enhanced permeability and retention (EPR) effect of tumor vessel.[11,12] The nanomaterials are designed as chromophores considering the characteristics of light emission to image tumor specifically and sensitively. The modification of specific ligands enables nanomaterials to target imaging; the dedicate structure can achieve more resonance to the laser beam triggering light excitation; the optimal surface areas provide drug delivery for precise treatment. Not only imaging of tumor but also immunotherapy and thermal therapy can be realized in presence of antibodies or photosensitizer agents.[13,14] Therefore, laser spectroscopic techniques coupled with nanomaterials can provide more possibilities for precision medicine and human survivals.[15]

The laser spectroscopy imaging techniques coupled with nanomaterials for cancer diagnosis, including Raman scattering, photoacoustic, fluorescent, infrared, and LIBS, are gaining attention. Owing to the localized surface plasmon resonance (LSPR), Raman scattering intensity could be greatly enhanced by magnitudes coupled with delicate nanomaterials, i.e., nanostars and nanospheres, which is also named surface-enhanced Raman scattering (SERS).[16,17] And the photoacoustic is a potential noninvasive imaging technique for cancer diagnosis and screen, which is subjected to the photothermal conversion capability of imaging agents.[18–20] The exogenous agents might penetrate deeper without the optical interference. Besides, the nanomaterials with near infrared (NIR) absorption also could display excellent imaging resolution at tumor site. Fluorescent nanomaterials that are excited to the NIR region or NIR II are commonly explored for deeper imaging.[21,22] The above laser spectroscopic imaging could achieve cancer diagnosis before or during surgery as a guidance. After intravenous injection of nanomaterials, the target location can be imaged *in vivo* noninvasively due to the improved fluorescence quantum yields (QYs), SERS enhancement factor or photoacoustic

efficiency. The nanomaterials with specific ligands are also capable of targeting designed tumor biomarkers. The handheld scanner, integrated with excitation and reception systems, enable image tumor margin *in situ* with the indication of nanomaterials. Therefore, the resected area can be scanned by *in situ* imaging system to determine whether the resection is clean. The operation of imaging system would be facile for surgeon, which do not require specific environment. For post-operative diagnosis, LIBS could be an assistant digital immunology method. The LIBS spectra include element information of tissue related to metabolism, which could delineate differences between the healthy and neoplasm.[23]

In this paper, we critically summarized several spectroscopic techniques coupled with nanomaterial to sensitively image tumor site including SERS, photoacoustic, fluorescent, and LIBS, respectively, in Fig. 1 (considering the infrared nanomaterials for imaging are universally in a way of fluorescence, which would not be discussed alone). Applications into cancer diagnosis mainly focus on the imaging of tumor *in vivo* noninvasively, or discriminations of cancer *in situ* and *ex vitro*. Different structures and compositions of nanomaterials would be presented together with their enhancement mechanisms considering the laser imaging principle. These summarized prominent studies, utilizing nanomaterials, inspire us that the laser spectroscopic techniques could offer supplementary information for surgeons during, before or after surgery. What's more, the multifunctional nanomaterials could bring us multimodality imaging and thermal therapy. The study of nanomaterials for imaging to cancer diagnose requires the efforts of material scientists, optometrists and physiologists, as well as physicians, among others. This review may provide some ideas for researchers in the field of optical-nanomaterials diagnostics.

2. SERS Imaging Nanoparticles

Elastic and inelastic collisions can occur after the interaction between photons and objectives causing light scattering.[27] During the process of elastic collision, the direction of moving photons is changed with maintained frequency while no energy is exchanged between photon and molecule, which is considered as Rayleigh scattering. On the contrary, photons accept the energy from the vibration and rotation of a molecule, changing the frequency, which is called inelastic collision forming Raman scattering.[28] Therefore, the frequency shift of different types of substance is distinctly subjected to its internally different structure. The frequency shift is the difference in the frequency of an original

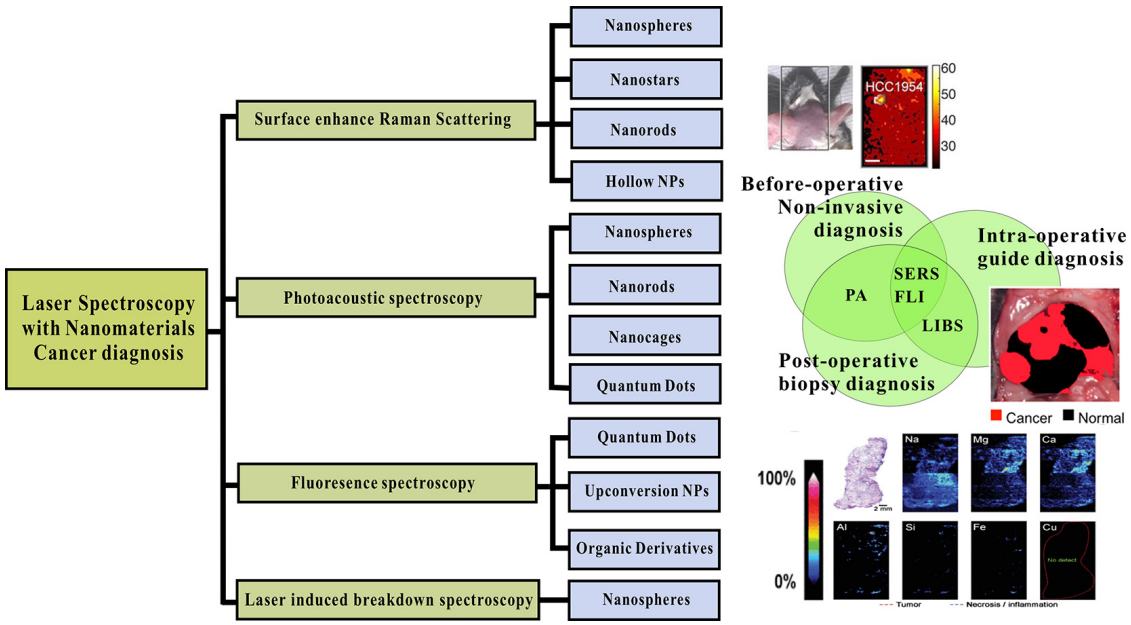

Source: Adapted from Refs. 24–26 with permission.

Fig. 1. The application of spectroscopic imaging techniques integrated with nanomaterials for cancer diagnosis.

excitation light source forming the unit as wavenumber (σ, cm^{-1}) that is irrelative to the type of the excitation light source.[29] Hence, the generation of Raman spectra is relevant to the substance, which has been used for the analysis of fatty acid in tumor micro- and macroenvironment,[30] brain tumor infiltration image,[31] and nucleic acid imaging of live-cell,[32] etc. However, spontaneous Raman scattering spectrum often accompanies interference of autofluorescence causing poor signal noise ratio, low sensitivity, and weak Raman signal. Subsequently, label-tagged Raman scattering spectroscopy relied on nanomaterials into tumor diagnosis is widely researched.

Raman imaging with SERS nanoparticles (NPs) is a highly prospective technology for the tumor diagnosis. SERS imaging has made many advances on preclinical research, especially imaging *in vivo* and *in situ*.[33,34] The NPs can be predominantly extravasated and uptaken by oncogenic and malignant tumors, thanks to passive EPR effect.[12] In addition, the NPs could be functionalized via specific ligands for active specific biomarker targets. Hence, those sensitive and specific SERS NPs have been used for the cancer diagnosis *in vivo*, *in situ*, and *ex vitro*. SERS is a technique based on "hotspot" area at the surface of noble metal NPs.[35] There are two mechanisms working for it. One is the surface plasmon resonances named as electromagnetic effect.[36] The electromagnetic field intensity at the surface of metal substrate will be significantly enhanced under the excitation of laser, which could amplify Raman scattering intensity. The other is chemical mechanism which is based on the interaction between micromolecules and electron at certain surface sites.[37] Therefore, the SERS effect is determined by the material,[38] geometry,[35] size, and nanogap of the noble metal NPs and incident laser.[39] To generate the hotspot area, the sandwich structure with interlayer inside is universally utilized, which is constructed by Raman report molecules between metal core and protective coating.[40]

2.1. *Core–shell hybrid nanospheres*

The core–molecule–shell structure is universally used, which could endow a gap inside. The extremely small Raman molecule as an interface generates a slit in the sandwich structure for plasmonic resonance. Thus, the scattering signal of the interior molecules could be enhanced by the electromagnetic field.[41] Campbell *et al.* orally injected sandwiched SERS NPs (gold core and silica shell, $Au@SiO_2$) into nude mice. The bio-distribution of NPs in liver, spleen, and stomach are imaged *ex vitro*.[42] The applications of $Au@SiO_2$ could be achieved *in vivo* due to the biocompatibility of silica. Ross *et al.* analyzed the inflammatory factor *in vivo* via $Au@SiO_2$.[43] Andreou *et al.* also utilized $Au@SiO_2$ to image liver tumor, which outlined the cancerous lesion of 250 μM that MRI couldn't reach.[25] It is the nanostructure that enhances the Raman scattering. Besides, the silver-coated gold (Au@Ag) nanostructure is universally applied into SERS effect. Except the core–shell structure, the hybrid substrate with superior extinction coefficient than the solo metal NPs could provide excellent SERS effect.[44,45] Chen *et al.* decorated three different alkyne tags on Au@Ag to implement three-channel imaging of live Hela cells at 2105, 2158 and 2212 cm^{-1}.[46] For the imaging *in vivo*, the silver surface might not be suitable due to the metal toxicity. To utilized the superior extinction coefficient of silver, an insight study using triple hybrid metal nanospheres (Au@MBN@Ag@Au) achieved ultrabright *in vivo* tumor SERS imaging in a $1\times1\,mm^2$ area (Fig. 2(a)).[47] This approach not only utilized the sandwich structure but also the triple hybrid-substrate, which significantly enhanced the sensitivity of SERS imaging *in vivo*.

2.2. *Nanostars*

Except the hybrid metal materials, the roughly spike structure is also important. The tips of NPs could concentrate the incident laser into a relative high density state, which could enhance the electromagnetic fields.[17] That's why the tringle pyramids,[48] nanostars,[17] and hollow nanostructures[49] are widely explored. The nanostars ($\sim$ 30 and 60 nm) could enhance Raman signal of tumor characteristic peaks (1067 and 1588 cm^{-1}) due to their sharp shape.[50] Later, Tian *et al.* achieved SERS imaging of lung tumor ($\sim$ 3 mm)*in vivo* with nanostars ($\sim$ 35 nm)[51] (Fig. 2(b)). The synthesis of nanostars is usually produced by seed-mediated generation. Thus, the hybrid metals are taken into account for the increase of SERS effect. Zeng *et al.* investigated the enhancement effect of Raman reporter (DTTC)-coupled $Ag_{core}@Au_{shell}$ nanostars ($\sim$ 74 nm)*in vivo*.[52] The signal of SERS NPs at tumor are stronger than Ag@Au nanostars and

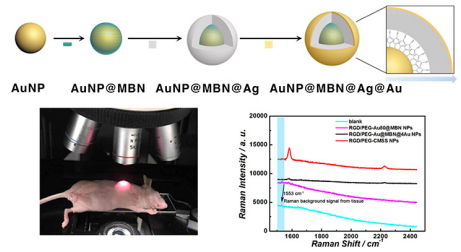

(a)

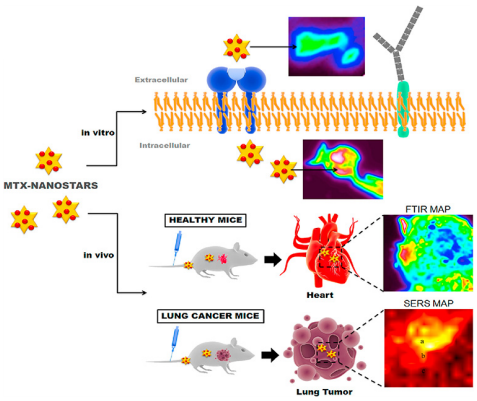

(b)

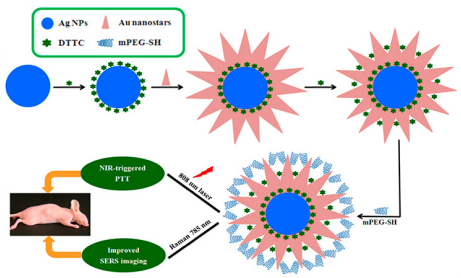

(c)

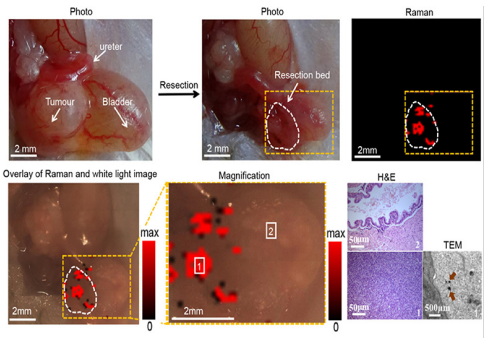

(d)

Source: Adapted from Refs. 47,51,52, and 64 with permission.

Fig. 2. (a) The double layer of Au@Ag@MBN@Au NPs. (b) The synthesis of nanostars and SERS image tumor *in vivo*. (c) Gold NPs mediated the synthesis of nanostars. (d) The CuS NPs accumulated in tumor during surgery in mice.

DTTC molecules. The above works display the feasibility of nanostars that could identify tumor *in vivo*. The injection of nanostars into tumor mice were accumulated at neoplasm region due the EPR effect. To further improve specificity of SERS imaging, the nanostars could be encapsulated with functional ligands. The specific SERS NPs could exhibit more distinguishable Raman spectra between tumor and normal tissue, compared with solo NPs. Nayak *et al.* also successfully detected and delineated pulmonary micrometastatic lesions as small as 200 μm utilizing nanostars conjugated antibody (Fig. 2(c)).[53] Furthermore, their team simultaneously monitored two biomarkers (EFGR and HER-2) to improve the sensitivity of bioimaging and tumor boundary identification. The image brain tumor *in vivo* through skull and *in situ* was completed.[24] The imaging depth could be improved via functional nanostars.

2.3. *Nanorods*

The various aspect ratios of nanorods (NRs) could be fabricated to concentrate photon via the shaped tips, which can adjust SERS enhancement effects.[54] A novel lysosome-targeted gold NR was successfully fabricated, which was capable of *in situ* SERS monitoring pH owing to specific ligand cysteine-hydroxyl merocyanine.[55] Besides, the multimodal imaging-guided photothermal therapy was achieved via the excellent absorption wavelength at the NIR "biological window".[56] The NIR absorption endows NRs with the capability of thermal conversion. Therefore, the NRs NPs are universally regarded as PA imaging agents at the same time. Jokerst *et al.* presented the ovarian cancer detection *in situ* with gold NRs as SERS guidance agnets.[57] The uncut tumor margin could be pointed out due to the EFR effect of NRs, which could prevent recurrence of cancer. The noninvasive PA imaging was also realized. The tunable hybrid core–shell structure of NRs also improves the SERS effect for imaging. The silver[58,59] or silica[60,61] layer are coated on the surface of gold core for enhance imaging sensitivity *ex vitro*.

2.4. *Hollow nanostructure*

The hollow nanostructure also could be applied into SERS enhancement. The interior gaps among hollow nanostructures generate electromagnetic field,

forming intraparticle hot spots.[49,62] Kang *et al.* synthesized rough NPs via silica core and Au@Ag hollow shell, which achieved tumor diagnosis *in vivo* with NIR property. He *et al.* also utilized the hollow Ag hybrid Au nanoshell, which could discriminate primary tumor tissues and metastases in mice model. The metastatic liver was about 0.18 mm, which indicated the prominent sensitivity.[63] Qiu *et al.* also composited NIR hollow CuS NPs that could enhance the Raman signal of imaging and were degradable under laser-induced photothermal effect[64] (Fig. 2(d)). They also achieved the SERS imaging as a surgery guidance during tumor section. The chemical enhancement mechanism dominantly works for this. The charge of Raman molecule was transferred into the hollow NPs, which induced plasmonic resonance.[65] It is the plasmon resonances that lie in the NIR which also make it penetrate deeper while imaging *in vivo*.

2.5. *NIR dyes-doped NPs*

The imaging depth is a crucial problem for *in vivo* imaging techniques. The Raman molecules are universally encapsulated in SERS NPs for emitting Raman signal (i.e., Rhodamine-6-G, Nile blue, 2-Napthalenethiol, etc.).[66] However, they are active in the UV/Vis range thus limited to image *in vivo*. To penetrate deeper, the Raman dyes with NIR region property are widely combined with SERS NPs. NIR dyes to provide a higher Raman scattering cross-section according to Raman transition in the electronically allowed state instead of virtual states. Animesh *et al.* utilized the core cyanine scaffold of tricarbocyanines as excitation of Raman signal in NIR region.[67] *In vivo* selective and stable detection of HER2-positive tumors was complemented in the mice model with scFv-conjugated CyNAMLA-381 gold NPs (AuNPs, 60 nm). Spaliviero *et al.* encapsulated AuNPs (60 nm) with resonant Raman reporter (IR780 perchlorate) and silica-PEG at surface.[68] The handheld Raman scanner enabled *in situ* Raman imaging of PC-3 lymph nodes metastasis for surgery guidance. The most significant is that the size of the lymph nodes in the mouse model is in short axis. The size of lymph node is even 10-fold smaller than human. Besides, the multiplexed imaging also could be realized via multiple dyes.[69]

As mentioned above, the property of SERS NPs for imaging *in vivo* or *in situ* provides a glimpse into superiority over currently clinical available imaging methods. It is the hotspot area inside NPs that directly affects the intensity of SERS.[35] Thus, for imaging *in vivo* and analysis *ex vitro*, the NPs could be optimized via material, geometry, Raman dyes, and choices of aptamers or antibodies. For the diagnosis *in situ* during resection surgery, the new Raman spectroscopy is also expected to be developed. Functionalities of shorter scanning time and deeper dimension even potential tomographic imaging are desired to be developed. The combinations of different imaging systems were universally considered as another solution to image deeper. Nicolson *et al.* combined SERS NPs (nanostars functionalized with cylic-RGDyk, 150 nm) with spatially offset Raman spectroscopy (SORS).[70] The deep-seated imaging *in vivo* through the intact skull for glioblastoma multiforme (GBM) tumors diagnosis was achieved. SORS offsets the point of laser excitation from the collection optics, which settle the depth limitations in the conventional Raman spectroscopy.[71] Hence, SORS integrated with SERS NPs could also display deeper layers in the turbid medium and biological tissue,[72] which could offer noninvasive imaging *in vivo*. In addition, higher tumor-to-background contrast is observed in comparison to those collected using conventional Raman imaging system. The NP-based SERS imaging technology offers the potential for intraoperative guidance even noninvasively comprehensive molecular imaging, and a complementary way to the current clinical gold standard of immunohistochemistry for tumor diagnosis.

3. Photoacoustic Imaging Nanoparticles

Photoacoustic imaging (PAI) is an emerging biomedical imaging technology. PAI is based on the photoacoustic effect. A continuous pulse laser with a width of nanoseconds or intensity modulation hits on tissue, which generates photoacoustic waves via the transfer from electronic energy into heat energy.[20] The partial pressure rises through instantaneous thermoelastic expansion and propagates in the form of ultrasound which then is detected by an ultrasonic transducer set up outside the tissue. According to the analog-to-digital conversion and data reconstruction, ultrasound is transformed into images. PAI displays deeper penetration and a higher spatial resolution image reflecting the

difference in tissue optical absorption thanks to the one-way propagation of light and detection of ultrasound.[73] Therefore, the PA signal is based on optical absorption of substrates.[20–74] PA effect for imaging varies with the light absorption properties of the tissues. Hence, the formation of tumor microvessels,[75] the level of blood oxygen saturation of the tissue,[76,77] and oxygen metabolism[78] can be obtained by PAI. These tumor microenvironment indices are related to the metabolism of hemoglobin. PAI displays the tumor metabolism in a nonradioactive way for cancer diagnosis, which is limited by PET, CT, and MRI. PAI could be categorized into three main methods: photoacoustic tomography (PAT) with wider bandwidth,[79] photoacoustic microscopy (PAM),[80] and photoacoustic endoscopy (PAE).[81] These techniques differ from the irradiated energy and penetration depth.[82,83]

The PA effect depends on the optical absorption. For PA imaging *in vivo*, the endogenous substances, like hemoglobin,[84] melanin,[85] water,[86] and lipids[87] related to tumor microenvironments, are ideal contrast agents. However, the inherent substances could generate a high PA background in living organisms, which makes PAI limited in biosensing and bioimaging. Therefore, some exogenous contrast agents, such as inorganic metal NPs and organic dyes, could improve PA signal to address the shortage of endogenous contrast agents.[88] Nanomaterials synthesized by metallic substrate, graphene or organic polymers have been investigated as contrast agents for PAI for cancer diagnosis *in vivo*.

3.1. *Nanospheres*

PAI is associated with photothermal conversion effect of the substrate due to PA effect. Therefore, metallic nanomaterials endow excellent high light-to-heat conversion. It is the LSPR that played a major role, which is produced on the surface of nanomaterials when the frequency of incident photons matches the frequency of electrons.[89] Gold nanomaterials are generally used for PA enhancement due to the excellent LSPR absorbance which is regulated by the size and morphology. Nguyen *et al.* wrapped AuNPs with PEG to enhance stability, solubility, and biocompatibility, which acquired optimized PA imaging of retinal and choroidal vessels on the rabbit after AuNPs-PEG injection.[90] As shown in Fig. 3(a), Du's team adjusted LSPR resonance of AuNPs to the NIR-II region via zwitterionic polypeptide (PMC), which intensified resonance effects and large dielectric difference between interlayers.[91] The PAI of MCF-7 tumor-bearing mice indicated PA amplitude with excellent enhancement thanks to the PMC@AuNP, of which tumor boundary could be delineated completely.

3.2. *Nanocages*

The gold nanocages (GNCs) are characterized by a single-crystal structure with hollow interiors and ultrathin porous walls.[92] GNCs also are ideal candidates as contrast agents for PAI in deeper biological tissues.[93] The LSPR peaks of GNCs can be easily and precisely tuned to wavelengths in the NIR range by the change of size or wall thickness. For *in vivo* study, Liu *et al.* synthesized the GNCs (30–40 nm) with organic dye680 and peptide targeting tumor protease MMP-2. The specific GNCs would be retained inside tumors for an extended period, in which the PA intensity ratio of 680:770 nm represented the MMP-2 expression.[94] Hence, the existence of GNCs could localize more tumor-infiltrating area, which could be clinically significant.

3.3. *Nanostars*

Nanostar-shaped NPs could be retained nicely in the tumor region subjected to the hydrodynamic size in biological medium around 100 nm. Beside, a high absorption coefficient in the NIR region could be obtained in the region.[95] Antoine *et al.* explored that the intertumoral delivery and retention of nanostars display an intense contrast *in vivo*.[96] Cheng *et al.* utilized nanostars to enhance the absorption efficiency and PA intensity, which was confirmed by monitoring PA signal in the tumor at 0, 6, 24, 48, 72, and 120 h post-injection (Fig. 3 (b)).[97] The phototherapy effect also could be improved due to the excellent LSPR of nanostars, which also confirm the enhanced PA effect.

3.4. *Nanorods*

Rod-shaped NPs exhibit intense and narrow absorption peaks for light in the far-red and NIR

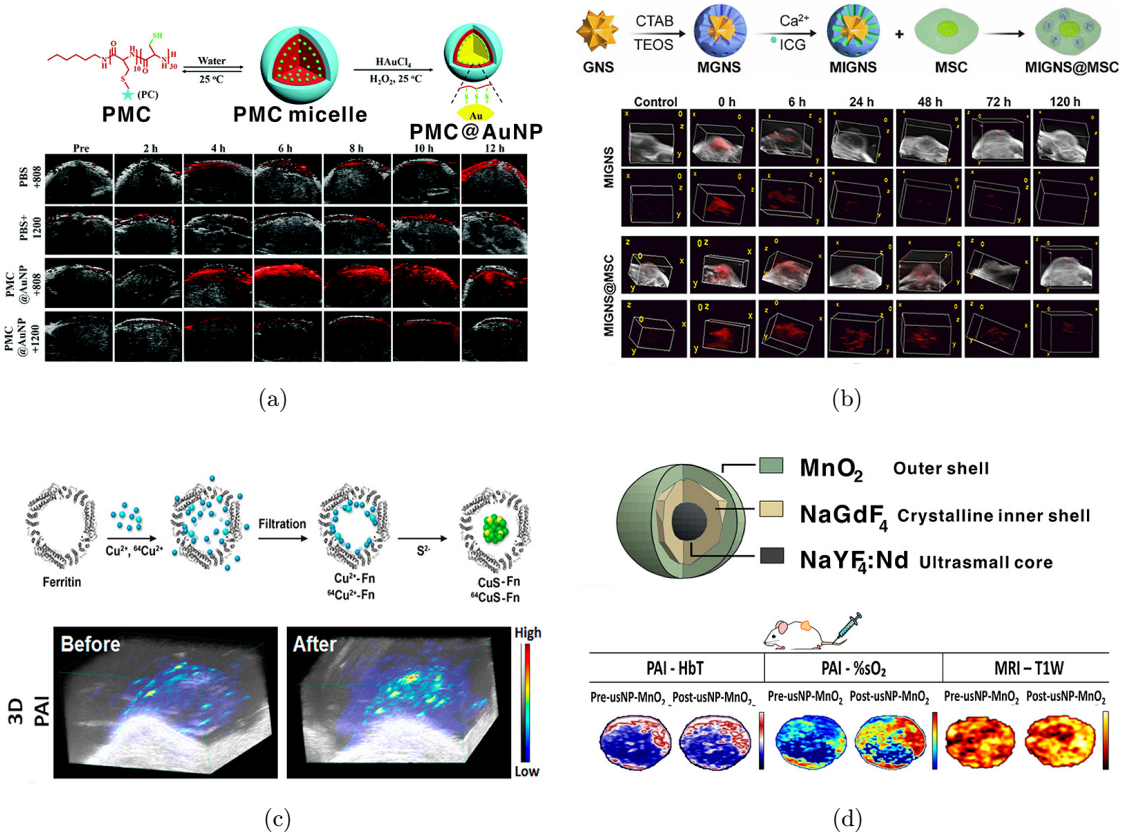

Fig. 3. (a) The design of PMC@AuNPs and PAI in tumor margin after intravenous injection. (b) The design of gold nanostars and PAI intratumoral distribution *in vivo*. (c) The MnO_2-coated ultrasmall NPs and indication of hypoxia in HNSCCs xenografts. (d) The synthesis process of CuS-Fn NCs and PAI and 3D PAI of tumor site. Adapted from Refs. 91, 97, 115, and 118 with permission.

wavelength regions, owing to the excitation of longitudinal plasmons.[98] The modulation of aspect (length to width) ratio of gold NRs (AuNRs) that could lead to a shift in their absorption spectrum toward the NIR and PA feature is universally studied in PAI *in vivo*.[99,100] In this wavelength regime, the light is able to penetrate fairly deep owing to low absorption and low scattering by tissue.[101] Li *et al.* found that the different aspect ratios of AuNRs with different light absorptions display distinct PA effect.[102] Chen *et al.* investigated that the smaller size of AuNRs (L: 49± 9 nm, W: 8±2 nm) with the same absorption and larger aspect ratio has more stable thermal stability and conversion efficiency, compared with the larger size of AuNRs (L: 120±17 nm, W: 18±4 nm).[103] The PA signal of smaller AuNRs at tumor site (∼ 1 cm) is even 4.5-fold stronger than the larger ones. Later, Cai *et al.* synthesized miniature hollow-structured AuNRs (L: ∼ 46 nm) which could exhibit 3.5 times stronger PA intensity and twofold accumulation in tumor than the larger ones (L: ∼ 105 nm).[104] There are some studies that explored different capping agents to reduce AuNRs with NIR or NIR II biowindow and enhance PA effect.[105,106] It could be noted that the AuNRs with tunable light absorption property could be the ideal PA contrast and thermal therapy agents.

3.5. *Quantum dots*

Quantum dots (QDs) consist of 2–10 nm nanocrystals with enhanced photostability, broad absorption and narrow symmetric emission spectra, large molar extinction coefficients, and high QY.[107] QDs are widely applied in PAI and fluorescent imaging owing to the photon yield proportional to the integral of the broadband absorption.[108] Transition metal chalcogenides (TMCs)-based nanomaterials, such as copper sulfide (CuS),[109] tungsten sulfide (WS_2),[110] molybdenum sulfide (MoS_2)[111] and so on due to energy band transitions are semiconductor nanocrystals with strong NIR absorption.[112,113] Especially, the CuS in the field of theranostic are

the low cost and intrinsic NIR absorption of CuS derived from energy band transitions instead of surface plasmon resonance. Li *et al.* constructed the copper bismuth sulfide NRs with broad and strong photo-absorption ranging from UV to NIR wavelengths.[114] What's more, the PA signal enhancement was apparently observed after 15 min post-injection even at three wavelengths. Wang *et al.* exhibited the PAT improvements of copper sulfide-ferritin nanocages (CuS-Fn NCs) for real-time *in vivo* PAI of entire tumors (Fig. 3(c)).[115] Besides, the CuS has been proven to facilitate the electron hole separation and transferring, during which $1O_2$ was generated.[116] Liu *et al.* also layered double hydroxide-CuS NPs as a versatile nanoplatform to achieve *in vivo* PAI of the tumor and kill cancer cells via subcellular ROS.[117] Generally, the CuS NPs could generate strong PA signal and high photothermal conversion efficiency. The ROS catalytic efficiency of CuS also makes it available for cancer therapy, which could monitor the tumor size and morphology during the chemical therapy.

The sensitivity of PAI could also be enhanced via peroxidase activity of metal ions like Fe and Mn in the tumor microenvironment due to acidosis, which could catalyze H_2O_2 into H_2O and O_2. Seshadri *et al.* encapsulated UCNPs with MnO_2, which improved the PAI response to the change of oxygen saturation *in vivo* at head and neck squamous cell carcinomas (HNSCCs) tumor site (Fig. 3(d)).[118] Chen *et al.* utilized the Fe^{3+} ions doped in polyvinyl pyrrolidone (PVP) and gallic acid and PVP to enhance photothermal efficiency.[119] Zhang's team also encapsulated Fe_3O_4 with CuS and photosensitizer to promote generation of ROS and sensitivity of PAI.[120] The generation of heat, energy conversion and a faster cycle of acoustic pressure could be amplified via iron oxide.[121]

The transition metal Pt as a kind of traditionally catalytic nanomaterials has the potential to be broadband PA agents due to their high-order longitudinal SPR mode located in the NIR zone.[122] In comparison with gold NPs, FePt NPs generate stronger photoacoustic signal, which was verified by Phan's work that explored the capacity of light-to-heat transformation *ex vitro*.[123] For PAI *in vivo*, Zhang *et al.* synthesized the two-dimensional (2D) PtAg nanosheets with stronger PA effect in NIR-II bio-window.[124] The functionalized PtAg nanosheets have strong PA performance with good permeability and retention effect at tumor sites for PAI of 4T1 tumor *in vivo* after 6 h injection. It is indicated that the plasmonic Pt is promising to be the element of novel photothermal treatment (PTT) and PA contrast agents for therapy and diagnosis of cancers in NIR-I or NIR-II bio-windows. Other transition metal elements also endow outstanding PA effect. An insight analysis reveals that antimonene (AM) with the unique thermal property including the morphology-related high interfacial thermal conductivity might interpret the high photothermal conversion efficiency and thus, the excellent photoacoustic performance.[125] Yu *et al.* display the superior PA signal of AM contrast agents at tumor site after 30 min post-injection.[126] Jin *et al.* also confirmed that the AM could modify the thermal efficiency of AuNPs, enhancing PA signal.[127]

3.6. *Graphene quantum dots*

Graphene QDs (GQDs) are a kind of quasi-0D carbon materials derived from graphene, which are universally applied into PA contrast agents. Owing to special $\pi - \pi$ conjugated bond, GQDs could deliver peptides, drugs or NPs.[128] Nie *et al.* endowed GQDs with the peroxidase-like activity with a nanozyme fragment (GQDzyme), which enhanced PA signal in the tumor H_2O_2 environment owing to the optical absorption and photothermal properties of nanozyme substrates ABTS.[129] The PA signal of GQDzyme was applied to image the tumor site as early as 2 h after the injection *in vivo*. To obtain excellent PA signal tumor area, the GQDs could also be loaded into the metal NPs substrate. Xuan *et al.* first exploited the N-doped GQDs that could acquire the absorption in NIR region with photothermal conversion efficiency of 62.53% *ex vitro*. Later, they modified AuNPs with GQDs, due to which the photothermal conversion efficiency increased up to 51.31% compared with sole AuNPs, which realized the tumor PAI *in vivo*.[130] The photothermal conversion efficiency of metal NPs could be improved via the modification of GQDs to enhance PAI contrast, i.e., gold nanostars[131] and AgNPs.[132]

The above research indicates that PAI combined with nanomaterials could enhance the PA contrast *ex vitro* and *in vivo*. Besides, PA contrast agent also can be cancer thermal therapy agents after diagnosis thanks to the excellent thermal conversion efficiency. For example, the nanomaterials with excellent LSPR absorption in NIR or NIR II region,

i.e., NRs and TMC. It is worth noting that the multiple imaging mode could be achieved via existence of cobalt, iron or manganese.[133] Zhao *et al.* achieved MRI and PAI *in vivo* with manganese NPs at the same time thanks to the excellent NIR absorption.[134] The MRI or CT could be integrated in this way to enhance resolution and sensitivity. Photo-acousticians are also committed to improving the spatial resolution from the PA devices.[135] Sun *et al.* utilized the advanced sparse imaging framework to perform PAI, which need few ultrasonic transducer elements with properties of high-speed and low-cost compared to traditional sparse reconstruction algorithms.[136] The multimodality optical fiber,[137,138] the optimization of reconstruction algorithm[139,140] and the kinds of transducer and combination of detectors[141,142] are mainly investigated.

4. Fluorescent Imaging Nanoparticles

Fluorescence is generated by energy emission from an excited electron returning to the ground state without a change in electron spin.[143] Therefore, the emission spectroscopy of fluorescence is dependent on the orbital of molecular, which could be utilized for quantification and qualification. Fluorescent imaging (FLI) has become a relatively mature analytical chemistry technique, but it still faces a challenge such as insufficient resolution and sensitivity of tissues or cells imaging. Nowadays, fluorescent nanomaterials with multifunctional sites have been promoted, which could achieve the cancer diagnosis *ex vitro*, *in situ*, and *in vivo*.

4.1. *Quantum dots*

The bio-window of QDs could be tuned around NIR region where the biological components do not substantially interfere with optical interrogation for deeper FLI. However, the size of universal QDs is suitable for passive retention, which easily causes high background and nonspecific accumulation. What's more, the removal of QDs is also affected by the relatively small size. To realize active target FLI, QDs could be functionalized with antibody or ligands. For instance, Seifalian *et al.* also utilized QDs linked with the HER2 antibody, which carried out NIR fluorescence imaging on SK-BR-3 cells (over expressing HER2) in contrast with MCF cells (under expressing HER2).[144] Carvalho *et al.* evaluated the glycol-phenotype on distinct types of breast cancer tissues *ex vitro* via the lectin that could recognize glucose and mannose residue outside the CdTe QDs.[145] The QDs could target towards cancer biomarker specifically and actively, which was confirmed by the FLI *ex vitro*. For QDs specific imaging *in vivo*, Hu *et al.* modified the QDs with RGD and BNN ligands (QDs-RGD-BNN) at the same time (Fig. 4(a)).[146] The tumor tissue uptake of QDs-RGD-BNN was higher than sole QDs. The dual target enables a higher ratio of tumor to background and faster response active to the tumor.

Since QDs are mainly hydrophobic, the capping agents are modified on the surface of QDs to provide sufficient biocompatibility and circulation times for tumor imaging. The polymers are universally considered owing to the superior surface modification. Gao *et al.* constructed a core–shell QDs encapsulated with triblock amphiphilic polymer to ameliorate aggregation and fluorescence.[147] This research displayed a better resolution compared with genetically encoded green fluorescent protein (GFP) tagging cells for *in vivo* cancer imaging universally. Kim *et al.* encapsulated CdTe/CdSe QDs with poly (lacticco-glycolic acid) (PLGA) to prepare stable and biocompatible QDs-loaded nanospheres for tumor imaging *in vivo* (Fig. 4(b)).[148] The QDs loaded in PLGA (135.0–162.3 nm) could be sensitively visualized through the tissue (> 1 mm) at tumor at a low concentration (20 μM) after 1 h post-injection. Both sensitivity and QYs are improved via polymers. An insight study informed that the zwitterionic copolymer as capped agents of QDs could lower toxicity, high fluorescence emission and controlled grafting rate, due to their demonstrated antifouling properties.[149] The hydrophobic groups wrapped QDs exposing hydrophilic groups, which enhance the biocompatibility.[150] Hence, these capping agents are tailored with great stability in aqueous media. And other functional moieties can be introduced on their surface.

To regulate the absorption and enhance QYs, the metal elements are applied into synthesis of QDs. The MoS_2 (34.55%, ~ 4.30 nm),[151] FeSe (40%, ~ 3 nm),[152] Ag_2Se (3.09%, ~ 3 nm),[153] Ag_2Te (2.3%, ~ 4 nm),[154] and Ag_2S (~ 6 nm)[155] are synthesized. The extinction coefficient of metal cores would influence the QYs of QDs. The FLI of tumor *in vivo* with the high ratio of signal to background could delineate tumor margin during surgery.

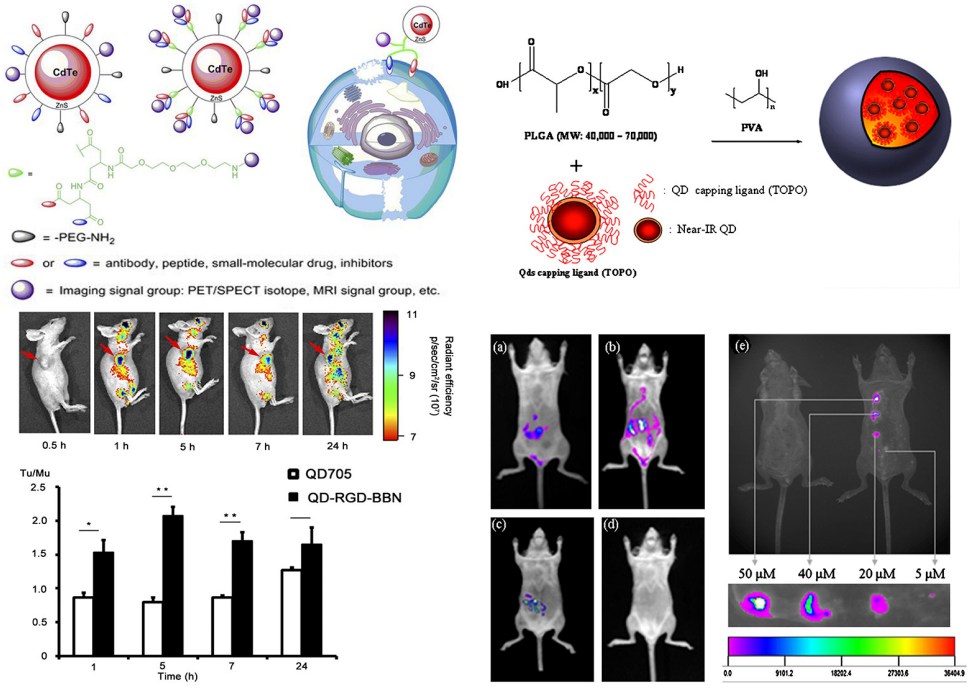

(a) (b)

Fig. 4. (a) The dual target QDs, functionalized with RGD and BBN peptide, enhance the sensitivity of FLI at tumor than EPR effect. (b) The PLGA capping agent improved the biocompatibility. Adapted from Refs. 144 and 146 with permission.

The enhanced uptake at tumor site also could be a noninvasive cancer diagnosis method due to the high QYs and absorbency of QDs. The concept of QDs design is generally a core–shell structure that is better for the fluorescence energy resonance transfer inside and the installation of specific ligands at the surface. CdTe, CdSe, and ZnSe are widely used. Whereas, the metal QDs consisting of cadmium, tellurium, and selenium elements limited the application into biomedical given the metal toxicity.[156] The carbon dots (CDs) are also generally applied into FLI due to the less cytotoxicity.[157]

4.2. *Carbon dots*

In the core of CDs, π-plasmon transitions contribute to optical absorption. At diverse surface sites, fluorescence ranging from the visible to near-IR was emitted according to photogenerated electrons and holes trapped and their associated radiative recombination.[158] The CDs (4–6 nm) wrapped with PEI capped agents could rapidly respond to the tumor margin in 30 min. Liu *et al.* synthesized a CD with red emission and high QYs (10.83% in water and 31.54% in ethanol).[159] The average diameter of 5.74 nm endows a high intratumorally accumulation and prolongs the circulation lifetime, which is perfectly suitable for brain glioma tumor imaging. The CDs could rapidly penetrate and reach the tumor site at 15 min after the injection (Fig. 5(a)). It is reported that the heteroatomic doping CDs can effectively tune the intrinsic properties for FLI.

The metal ions play as a catalyst in the synthesis of CDs with varied QYs. As shown in Fig. 5(b), Hua *et al.* prepared Ag-/Cu-/Pt- and Fe-/Pd-/Ni-doped CDs, respectively, with the red fluorescence (QY of 45.6% in dimethyl sulfoxide, DMSO).[160] Bao *et al.* newly developed sulfur- and nitrogen-doped NIR CDs with a high ratio of signal to background at tumor in 3 h post-injection.[161] Su *et al.* utilized hafnium-doped CDs (HfCDs, $\sim$ 3.76 nm) achieving rapid imaging in 1 min for tumor location (Fig. 5(c)).[162]

For higher tumor uptake, the specific ligand could functionalize the CDs. Karakoçak *et al.* grafted hyaluronic acid covalently, a natural ligand of CD44 receptors, on nitrogen-doped CDs (nCQDs) to image CD44-specific tumors *ex vivo*. The heteroatomic doping CDs and specific ligands realized sensitive tumor delineation.[163] For FIL *in vivo*, Wang *et al.* achieved CDs active targeting with FA, which penetrated liver tumor tissue and skin with

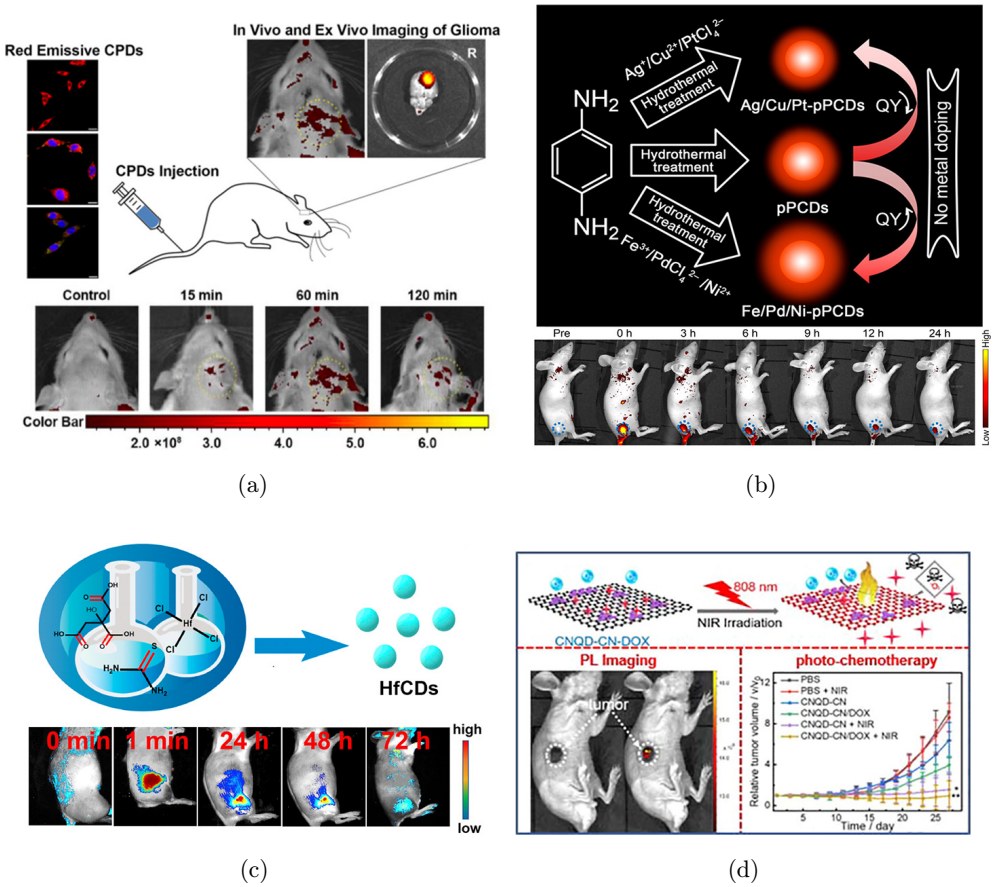

Source: Adapted from Refs. 162,165,168, and 169 with permission.

Fig. 5. (a) Red emissive CDs are suitable for brain glioma tumor imaging. (b) The Ag-/Cu-/Pt- and Fe-/Pd-/Ni-doped CDs, respectively, with the red fluorescence. (c) The Hf-doped CDs respond fast in tumor region. (d) The design of graphitic carbon nanomaterials.

enhanced fluorescence.[164] What's more, the graphitic carbon nanomaterials are applied into tumor FLI *in vivo* and *ex vivo* (Fig. 5(d)).[165–167] Owing to the large planar structure of graphene, it is reported that the successful synthesis of GQDs with strong absorbance at NIR or NIR II region could improve QY and thermal conversion. The dual modality imaging might be integrated.

4.3. *Upconversion NPs*

The UCNPs could convert longer wavelength radiation (e.g., NIR light) into a shorter wavelength fluorescence (e.g., visible light). NIR light avoids damage to biological tissues with deeper penetration compared with ultraviolet and visible light.[170] Thus, some fluorescent probes utilizing UCNPs have been applied into tumor biomarker detection and imaging. The process of successive electronic transitions inside lanthanide ions in multiple excited states brings about the photon upconversion. The lattice of a crystalline solid provides a prerequisite for diverse energy transfer.[171] Therefore, the crystal field is essential for lanthanide energy transfer as the emission and absorption bands of lanthanide ions are so narrow that it is unfavorable to the spectral overlap.[172] Besides, the host lattice of a field could affect the spectral position of optical transition which could satisfy resonance conditions.[173]

Hexagonal-phase (β-phase) $NaYF_4$ is one of the most efficient UCNPs host materials under 980 nm excitation and is universally doped with Yb-Er or Yb-Tm rare-earth ion couples. Water soluble UCNPs are traditionally assembled with oleic acid to acquire hydrophilic (Fig. 6(a)).[174] For active targeting, the UCNPs could be functionalized with antibodies or ligands (i.e., carcinoembryonic

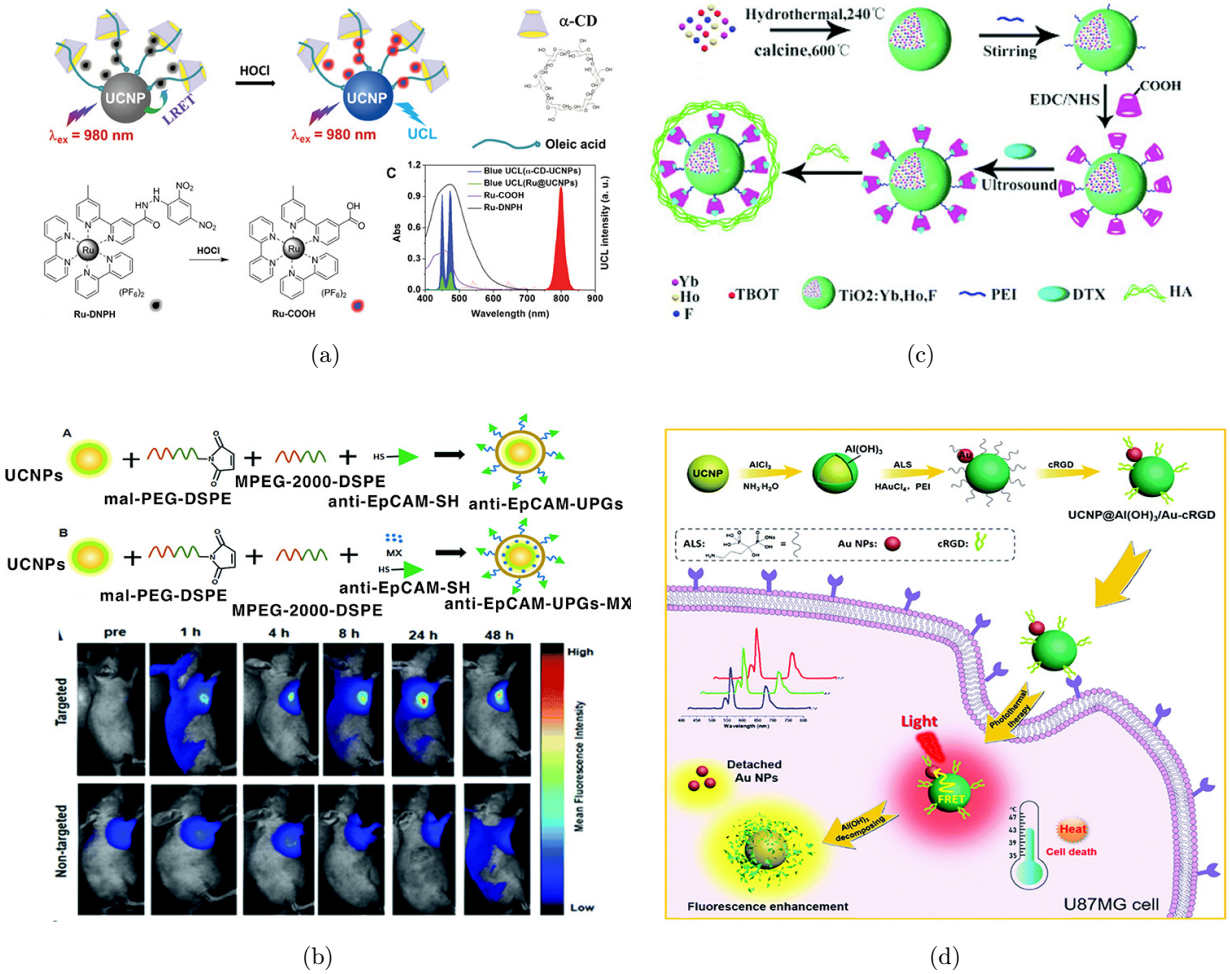

Fig. 6. (a) The oleic acids as capping agent of UCNPs. (b) The antibody of EpCAM functionalizes UCNPs. (c) The design of TiO_2 as the core of UCNPs. (d) $Al(OH)_3$ and AuNPs as the shell layer of UCNPs. Adapted from Refs. 179, 181, and 184 with permission.

antigen,[175] EphA2,[176] and peptides RGD10-NGR9,[177] etc.) to excite strong fluorescence for tumor cells imaging without interference of auto-fluorescence. These laser sources in the NIR region emit sensitive fluorescence visibly. For FLI *in vivo*, Zhang *et al.* demonstrated the capability of $NaYF_4$: Yb-Er UCNPs that functionalized with ConA recognizing high mannose glycoform cancer cells acquiring stable fluorescence*ex vitro*and *in vivo*.[178] Han *et al.* also realized the hepatocellular carcinoma imaging with EpCAM antibody-linked UCNPs in 1 h post-injection (Fig. 6(b)).[179]

The TiO_2 is universally considered as a core due to its high electron hole pair separation and absorption intensity, which laid a foundation for constructing visible. Yu *et al.* employ the incorporation of an anatase titanium dioxide ($aTiO_2$) photosensitizer as a spacer and exploit the LSPR properties of the Au core. The LSPR-derived near-field enhancement induces a threefold boost of upconversion emissions, which are re-absorbed by neighboring $aTiO_2$ and Au nanocomponents.[180] Zhou *et al.* utilized TiO_2 as the core of UCNPs which built a multifunctional platform for laser-induced FLI and therapy. The fluorescence intensity of tumor contrasted with normal tissue *in vivo* was obviously high (Fig. 6(c)).[181]

More nanohybrid UCNPs were synthesized for dual imaging and enhancing fluorescence. The UCNPs ($NaYF_4$) doped with Gd^{3+} and RGD display excellent high contrast between tumor and the surrounding normal tissues in 15 min after the injection *in vivo*.[182] The Nd^{3+}-doped UCNPs were synthesized as a core–shell structure showing a bright visible emission upon excitation at the NIR.[183] These metal label UCNPs could be the MRI

or CT contrast agents at the same time. For FLI and photo therapy at the same time owing to the excellent fluorescence energy transfer efficiency, the $Al(OH)_3$ and gold layer (Fig. 6(d)),[184] mesoporous silica-coated gold NR (AuNR@mS),[185] graphitic carbon nitride QDs,[186] and Mn-$Ca_3(PO_4)_2$ (MnCaP) layer[187] are taken into consideration. These delicate structures endow the UCNPs with enhanced thermal conversions or resonance signal.

Upconversion luminescence endows UCNPs promising as fluorescent bioimaging probes with attractive features, such as large penetration depth and no autofluorescence from biological samples. Integrated with some metal NPs or photosensitizers, multimodal imaging systems or multifunctional tools could be synthesized. As a result, UCNPs have emerged as novel agents for tumor diagnosis and therapy.

4.4. *Organic dyes derivatives*

Organic fluorophores of dyes, with properties of biocompatibility, spectral tunability, enhanced contrast, chemical and colloidal stability, are now becoming increasingly popular for fluorescent diagnosis and imaging. The photoluminescence of small molecules is closely related to their chemical structures. The special structure emitting fluorescence under laser excitation is constructed through π interactions, which is associated with π–π stacking,

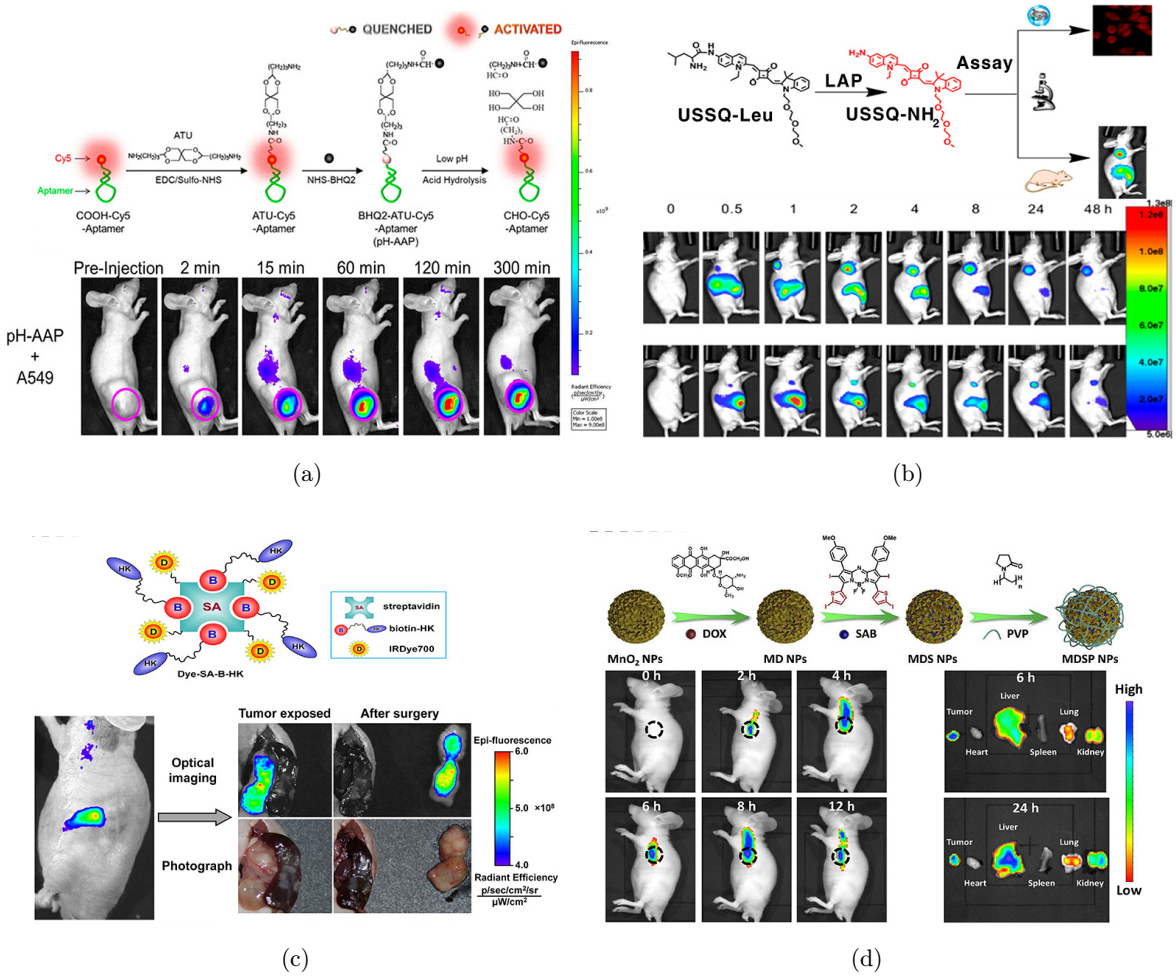

Source: Adapted from Refs.197–200 with permission.

Fig. 7. (a) The Cy5 pH-activatable aptamer probe (pH-AAP) and its acid-response at A549 grafted tumor site. (b) The OEG-functionalized squaraine NIR probe (USSQ-Leu) for leucine aminopeptidase (LAP) detection with high contrast in 1 h after intravenous injection. (c) The integrin $\alpha v\beta 6$-targeted NIR phthalocyanine dye-labeled agent (Dye-SA-B-HK) for surgery guidance. (d) The tumor hypoxia responsive MnO_2 doped with aza-BODIPY and photosensitizer for tumor diagnosis and thermal therapy.

Table 1. The applications of the main fluorescent organic dyes and their derived nanomaterials for cancer diagnosis.

Type	Ref.	Name	Extra agents	Specific targets	*Ex vitro* and *vivo* studies	Application
Cyanine	201	ICG	—	EPR effect of tumor	*In vivo* surgery	FLI of hepatocellular carcinoma (HCG) during surgery guidance
	202	Heptamethine indocyanine dye (IR-780 iodide)	—	EPR effect	MCF-7 cells; pigs and mice	FLI of sentinel lymph nodes
	197	Cyanine 5.5	Matrix metalloprotease-9 (MMP-9) connected with Fe_3O_4 NPs and ANNA pH dyes	Response to extracellular pH change at tumor sites	LS280 cells; LS180 tumor xenografts in tumor-bearing mice	FLI of colon adenocarcinoma (Fig. 7(a))
	203	CyA	Cycle peptide (RGD)	High affinity to $\alpha_v\beta_3$ integrins	MDA-MB-231, A549, U87; xenografts in tumor-bearing mice	FLI of metastatic tumors *in vivo*
Squararine	204	SQ-L	Liposome	EPR effect	MCF-7; MCF-7 cells xenografts in tumor-bearing mice	Dual modality of FLI and PAI
	205	SQ-BSA	Bovine serum albumin	EPR effect	KB cells, A549 KB xenografts tumor	FLI and PTT
	206	D1-micelle	Micelle: Pluronic F-127	EPR effect	Huh7 cells	Dual modality of FLI and PAI
	198	USSQ-Leu	L-leucine moiety and triethylene glycol (OEG)	Detect Leucine aminopeptidase (LAP) inside cells	HepG2 (High LAP), LO_2 (low LAP) L929 cells (LAP negative); HepG2 xenograft tumor model	FLI of LAP-overexpressed tumors *in vivo* (Fig. 7(b))
Phthalocyanines	207	ATF-HSA:CPZ	Human serum albumin (HSA) fused with the amino-terminal fragment of urokinase	EPR and specificity to urokinase receptor (uPAR) in many tumors	H1299 (positive) and HELF (negative) cells; H22 mouse model	FLI and PTT of tumor sites

Table 1. (*Continued*)

Type	Ref.	Name	Extra agents	Specific targets	*Ex vitro* and *vivo* studies	Application
	199	Dye-SA-B-HK	HK peptide sequence: RGDLATLRQLAQEDGVVGVRK	High selectivity and specificity to integrin $\alpha\nu\beta6$	BxPC-3 cells; BxPC-3 xenograft tumor model	FLI of pancreatic cancer during surgery and PTT drug (Fig. 7(c))
	208	IRD-aCD206	Monoclonal antibody (anti-CD206)	Targeted to tumor-associated macrophages	4T1 murine breast cancer and RAW264.7 cells	FLI and photoimmunotherapy
BODIPY	209	M-BODIPY-GSH and C-BODIPY-GSH	GSH moiety	Cancer-specific γ-Glutamyltrans peptidase (GTT)	HUVEC (negative), OVCAR5 and SKOV3 (positive)	FLI of living ovarian cancer cells
	210	BYD	2-Pyridone	EPR and ROS	HeLa cells; HeLa tumor mice model	FLI, PAI, and PTT of tumor
	211	BDP 2−7	—	EPR and pH response	HeLa cells; mice with U14 tumor	FLI, PA, CT, and PTT of tumor sites
	200	MDSP NPs	Anticancer drug-Doxorubicin (DOX) and MnO_2 NPs	EPR	HCT 116 cells; HCT 116 cells tumor model mice	FLI, PA, and PTT of tumor sites (Fig. 7(d))

Notes: *Abbreviation: GSH: the reduced glutathione; BSA: bovine serum albumin; RGD: the amino acid sequences; Leu: leucine; MCF-7, MDA-MB-231: human breast cancer cell line; LS280 and LS180: human colon adenocarcinoma cell line; Huh7 and HepG2: human hepatoma cell line; LO2 (Low LAP)H1299: human nonsmall adenocarcinoma; A549: human lung cancer cell line; U87: human astroglioma cells; KB: human oral epithelial cancer cells; L929: mouse fibroblasts; HELF: human embryonic lung fibroblasts; H22: mouse hepatoma cells; BxPC-3: human pancreatic adenocarcinoma cells*in situ*; HUVEC: human umbilical vein endothelial cells; OVCAR5: human ovarian adenocarcinoma cells; SKOV3: human ovarian cancer cells; 4T1 murine breast cancer cells; HeLa: human cervical cancer cells; HCT 116: human colon cancer cells.

electrostatic, hydrogen-bonding, hydrophobic/hydrophilic, and van der Waals.[188,189] It is the energy gap (energy separation between the highest occupied molecular orbital and lowest unoccupied molecular orbital) that controlled the fluorescent intensity. Organic fluorescent dyes are mainly categorized into four kinds: cyanine dyes, squaraine derivatives, phthalocyanines and porphyrin derivatives, and borondipyrromethane (BODIPY) dyes.

Indocyanine green (ICG) belongs to cyanine dyes that are small organic molecules with two aromatic nitrogen-containing heterocycles linked by a polymethine bridge, which has been approved as a contrast agent for years. Squaraines (SQ) consist of an oxocy-clobutenolate core with aromatic or heterocyclic components that (electron-donating or -withdrawing) are attached to the central squarate moiety which plays a major role in the photophysical properties of the dye.[190] The design of SQ dyes challenges the water solubility due to the structure of large and planar hydrophobic π-conjugation. The union of four pyrrole subunits assembled through nitrogen atoms constructs the central skeletons of phthalocyanines. Therefore, a series of thermally and chemically stable porphyrin derivatives have been synthesized centered on 2D 18 π-electron aromatics, which results from the electronic delocalization of π-electrons supporting intense electromagnetic radiation.[191] BODIPY dyes have a general structure of 4,4′-difluoro-4-bora-3a, 4a-diaza-s-indacene and sharp fluorescence with high QY and excellent thermal and photochemical stability.[192] Applications of some organic dyes and their integration with nanomaterials to tumor diagnosis are summarized in Table 1.

The FLI imaging could discriminate tumor margin before and during surgery. The resected tissue could also be scanned via fluorescent confocal microscopy as an immunology diagnosis method. What's more, the energy transfer of some nanomaterials (i.e., QDs[193]) could be the trigger of some photosensitizers to induce cancer cell apoptosis. The other (i.e., GQDs and CDs) could deliver cancer drug. More importantly, the tumor environment responsive nanomaterials (i.e., pH[194] and ROS[195,196]) could also be designed for FLI and photodynamic therapy (PDT). Therefore, functional fluorescent nanomaterials could be developed for simultaneous diagnosis *in vivo* and therapy of cancer.

5. Laser-Induced Breakdown Spectroscopy Imaging

LIBS is a chemical analysis technology based on plasma plume produced by pulsive laser ablating on materials.[212] Under the condition of high laser power density, a few micrograms of material on the surface are instantly heated to 10,000°C and ejected to form a visible and extremely bright plasma within a very short time.[213,214] These plasmas, consisting of excited atoms or ions, will quickly cool down at the end of the laser pulse which is the process of the excited atoms or ions returning from the high energy state to the low energy state and emitting optical radiation with their characteristics.[215,216] The surface of an object absorbs the energy of the laser and converts it into the form of heat conduction. The heat diffuses in the object, which ultimately leads to a series of changes in the optical properties of the object. After the intense pulsed laser is focused, the material will be broken down, which leads to bremsstrahlung and composite radiation at the beginning.[23] The disappearance time of the radiation is not the same for different objects. Then there is plasma radiation when the plasma is expanded and cooled to produce the plasma spectrum,[217] which disappears in a short time. Therefore, the ablation of different materials is distinct, which results in the distinctive formation of plasma and optical radiation. High-resolution detectors can detect and analyze these spectral radiations that obtain information on the elemental composition of matter.[218]

There are some significant advantages that make LIBS applicable in tissue detection and imaging. The need for sample preparation is little, which makes LIBS a fast way in clinical diagnosis even during the surgery operation[219]; versatility in all media makes it feasible in blood tumor diagnosis[220]; with the abilities of spatial resolution of 100 μm and simultaneous determination of multiple elements, it can obtain a comprehensive element distribution map of tissues and establish 2D and 3D tissue element imaging.[221]

LIBS system has been applied into some analysis of tissues, such as cholesterol gallstones,[222] malignant colon tissues,[223] kidney stones,[224] and carious teeth.[225,226] For the LIBS of tissue imaging, Moncayo *et al.* mapped the skin sample with a step size of 50 μm, which indicated the discrepancy of elements between normal and neoplastic skin tissues

(Fig. 8(a)).[227] Lin *et al.* also achieved LIBS *exvivo*3D elemental imaging of mouse brain tissue block layer by layer.[228] Chio *et al.* realized direct high spatial resolution (15 μm) LIBS imaging of cutaneous melanoma using a UV fs-laser with no pretreatment of sample, which identified latent tumor and inflammatory cells.[229] Besides, Yin *et al.* delineated the human lung tumor boundary based on multielement and molecular fragments with LIBS, which is clinically significant (Fig. 8(b)).[26] The LIBS imaging of tissues provides more detailed information that the hematoxylin and eosin staining (HES) method lacks. The distribution and intensity of elements are displayed distinctly among healthy normal, inflammatory and cancer tissues due to discrepancy of biological metabolism process.

The NPs are usually applied in LIBS imaging due to the small size NPs (< 12 nm) with the ability of accumulation and penetration and less toxicity, which results from the elimination through kidney.[230] Sancey *et al.* first achieved the distribution of Gd small NPs in the mouse kidney via LIBS elemental mapping with vertical resolution of 100 μM and lateral resolution of 10 μM.[231,232] Gimenez *et al.* first provided 3D Gd NPs imaging at the entire-organ scale, which enabled a resolution of $\sim 10\,\mu$m in all dimensions.[221] The Gd NPs accumulated at tumor site also could delineate the tumor margin and also could be realized via LIBS mapping (Fig. 8(c)).[231] However, the enhanced sensitivity has not been clarified, which deserves to be studied.

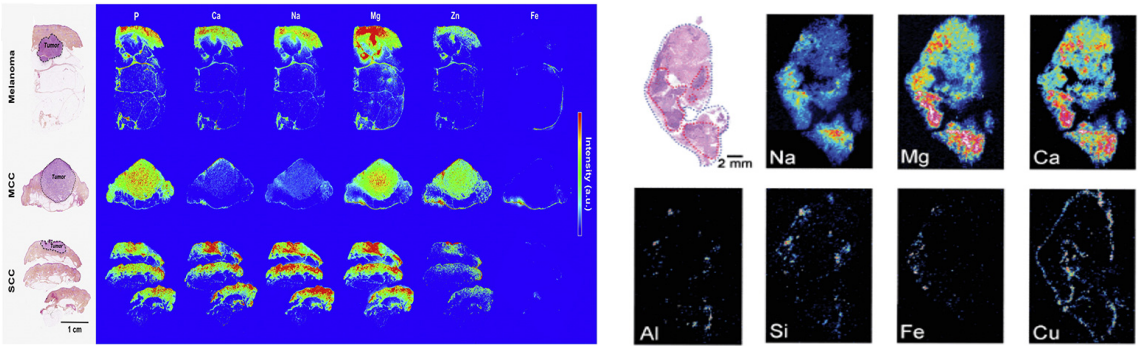

(a) (b)

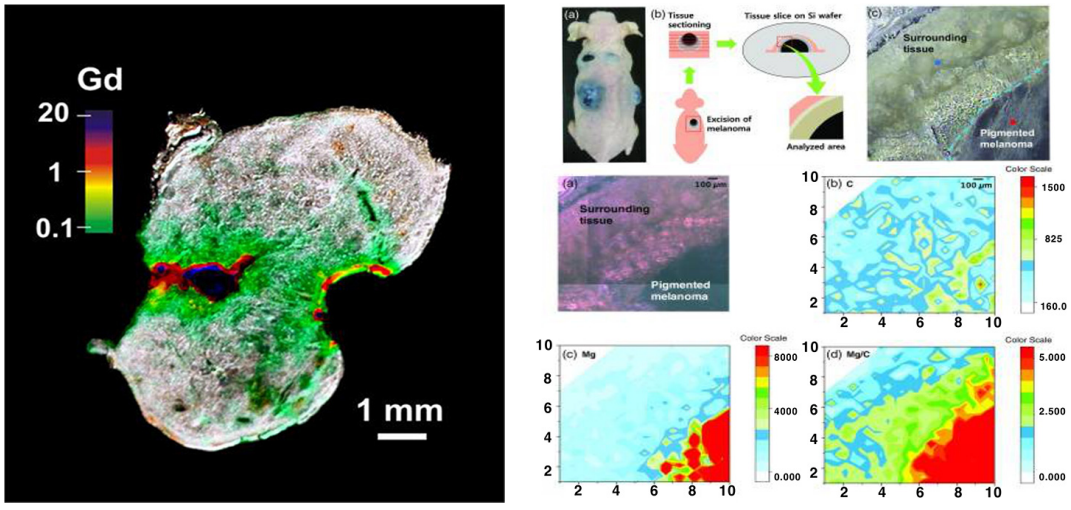

(c) (d)

Source: Adapted from Refs. 26, 227, 231, and 233 with permission.

Fig. 8. (a) Comparison of LIBS imaging and HES of skin cancer: melanoma metastasis, merkel-cell carcinoma (MCC), and squamous cell carcinoma (SCC). (b) LIBS mapping of elemental discrepancy between human tumor and normal lung tissue. (c) The *in situ* LIBS mapping of skin cancer. (d) LIBS mapping of Gd NPs distribution at tumor sites.

The samples in the above studies were processed via either epoxy-embedded or paraffin-embedded. In this way, LIBS could be a supplementary method for HES diagnosis after removal of potential tumor tissues. What's more, the LIBS could distinguish the discrepancy of tumor and normal tissue, which makes it an available diagnosis technique during surgery. Moon *et al.* mapped the intensity ratio of Mg to C in the fresh removal cutaneous melanoma tissue without any treatments *in situ* (Fig. 8(d)).[233] They found that when incorporated into the existing micrographic surgery procedure, fs-LIBS could be a useful tool for histopathologic interpretation of skin cancer possibly with significant reduction of histologic examination time.

Therefore, we find that the LIBS imaging of biological tissue for the cancer diagnosis during the intraoperative or post-operative is feasible. And the application of LIBS into tumor tissue imaging combined with NPs might improve the accuracy of tumor boundary delineation due to the penetration and retention characteristics of NPs at the tumor site. However, the enhanced sensitivity of NPs in LIBS imaging at tumor site has not been reported, to the best of our knowledge. Besides, the spatial resolution and damage to samples are also critical. The diameter of a crater caused by laser determines both lateral and axial resolution, while the laser energy relates to the spectral intensity of elements. What's more, LIBS can obtain the multivariate information of the sample at a point in one scan. Chemometric methods integrated with LIBS cloud help extract significant, distinctive, and specific spectra from the spectrums generated from normal and cancerous tissue, which promotes discrimination of samples based on the model established and validated before.[234–236] Further studies should consider the relationship between stages of cancer and the difference in elemental distribution. Besides, the integration of classification models might provide better results. Hence, there is still great potential for application of LIBS imaging in tumor diagnosis, which is worth exploring.

From the above research, the LIBS imaging for tumor diagnosis could be achieved during the intraoperative or post-operative. The LIBS imaging of tissue almost focuses on the paraffin-embedded samples, which could be a digital immunodiagnostic method. And for the intraoperative cancer diagnosis, a laser knife could be used, which could ablate tissue leading to the ejection of plasma. The spectrometer could be placed properly for the acquisition. The tumor boundary is identified by algorithm technology based on the raw data or principal component analysis (PCA) processed data, which can be interfered with by the condition of samples. Therefore, more LIBS mapping for tumor diagnosis should concentrate on direct analysis without pretreatment. On the other hand, the accuracy of different models recognizing cancer types and stages are distinct, hence the selection and establishment of models are also important. And the more comprehensive samples and data, the more accurate discrimination.

6. Challenges of the Application

Despite the progresses described above, some challenges need to be acknowledged and addressed. For SERS imaging *in vivo*, the tissue penetration depth is limited under the conventional short wavelength excitation light. And the imaging time is crucial for the surgery guidance, thus the longer integration time of SERS should be improved by an efficient CCD detector and the optimal nanomaterials. Fluorescent imaging is a relatively mature technique especially coupled with nanomaterial. However, the multidimensional fluorescent imaging systems are significant for cancer diagnosis *in vivo*, *in situ*, and *ex vitro* to avoid tumor recurrence and misdiagnosis. PAI is based on the PA effect. The sensitivity of PAI *in vivo* could be disrupted by surrounding thermal noises. And the algorithms for collection discrimination and feature extraction of PA signals are still worthy of a progressive enhancement. For the imaging and biopsy *ex vitro*, LIBS would generate the ablation damage to the samples and the quantitative algorithm needs to be improved in precision and accuracy. The above problems are required to be clarified. In the future, laser spectroscopic techniques coupled with nanomaterials could supplement the shortages of traditional clinical imaging techniques. In addition to the limitation of the laser spectroscopic imaging techniques, the nanomaterials should possess selective accumulation, high efficiency, and photostability. The preclinical and clinical assessments are crucial to understand the physical and chemical properties.

It is necessary to understand the complex systems and pathways within organisms to expand the applications of imaging *in vivo* and *in situ*. The

clinical translation will be hindered by fundamental limitations of human physiology. For instance, the silver NPs endow excellent absorption coefficient resulting in a stronger SERS effect but are toxic to humans; the larger size of noble metal nanomaterials (about 100 nm) with high efficiency isn't easily metabolized causing unknown risk to health[11,230]; the nanomaterials functionalized with specific ligands whether will be retained in the human body is still to be verified. How to ensure the nanomaterials could have a rapid response, retention time in the appropriate range and excellent renal clearance efficiency, bringing a good signal-to-noise ratio after intravenous injection into humans is a huge challenge. What's more, preclinical imaging in experimental animal models requires numerous tests to start clinical studies. Besides, for the cancer diagnosis *in situ*, it's hard to realize the comprehensive visualization of specific structure during surgery without clinically approved SERS and NIR nanomaterials. We summarized the advantages and limitations of laser spectroscopic imaging techniques coupled with nanomaterials in Table S2, compared with the traditional imaging methods in Table S1.

Nanomaterials can be used as therapeutic drugs in addition to amplification of signals as luminescent chromophores. The efficient delivery of biological molecular drugs and localized input of mechanical and electromagnetic waves is critical for multifunctional nanomaterials. Cancer metabolism is also a potential target for the nanomedicine treatment. For example, the upregulated ROS levels are present in solid tumor tissues, which promote tumorigenesis, progression, and tumor survival.[237] Thus, ROS-generating agents are being developed to disrupt cellular self-adaptation mechanisms and induce cell death, such as PDT and chemodynamic therapy (CDT). The PDT utilities light-activated photosensitizers are capable of converting oxygen (O_2) to ROS,[238] whereas CDT takes advantage of an *in situ* Fenton or Fenton-like reaction between hydrogen peroxide (H_2O_2) and catalysts to generate cytotoxic hydroxyl radical (·OH).[239] Besides, normal mammalian cells get ATP by mitochondrial oxidativephosphorylation (OXPHOS) and glycolysis. Cancer cells get ATP mostly by glycolysis instead of OXPHOS despite having sufficient oxygen.[240] Since glucose oxidase-mediated glycolysis is oxygen-dependent, the cascade reaction faces the challenge of a hypoxic tumor microenvironment. Metal NPs encapsulated with glucose oxidase and prodrugs (hyaluronic acid,[241] hemoglobinor[242] or tirapazamine,[243] respectively) were constructed as cascade nanodrugs for glucose consumption and peroxidase reaction. The cascade nanomaterials exhibit high efficiency for tumor suppression and provide an effective strategy for oxygen-mediated synergistic starvation therapy and CDT. For tumor microenvironment, metabolic pathways or metabolites, different drugs can be loaded on nanomaterials. Cancer researchers have extensively investigated the potential of various nanomaterials in cancer therapy. A variety of drugs integrated with nanomaterials have been studied for cancer treatment. Multiple therapeutic strategies have been analyzed, such as encapsulation of drugs, targeting glucose metabolism in tumor cells, enzymes responsible for cancer metabolism, and many others.

A combination of tumor metabolic features for imaging diagnosis and therapy is a potential way for precision medicine. In addition, cascade therapies allow for a more rapid target elimination to avoid recurrence. The composition, structure, and biocompatibility of nanomaterials and drug stability need to be addressed. In a word, further efforts and multidisciplinary cooperation are deserved to be paid among biologists, chemists and surgery specialists. The multifunctional nanomaterials can offer more efficient and accurate cancer diagnosis to achieve better surgical outcomes.

7. Conclusion and Perspectives

In this review, we have summarized several spectroscopic techniques discussing their working principles, applications of imaging and cancer diagnosis. These laser spectroscopic imaging techniques coupled with nanomaterials exhibit more accurate and specific diagnosis even in the deeper tissues. For the cancer diagnosis, we classify the scope of application of these spectroscopic techniques in three directions: before-operative, intraoperative, and post-operative.

For the cancer screening before operation, real time and noninvasive diagnosis is critical. Due to the acoustic effect, PAI has an advantage in penetration depth, which has been studied to imaging tissues real-time and noninvasively.[244] SERS and FLI, integrated with NPs, also could generate the

corresponding discrepancies between tumor and normal sites *in vivo* and *in situ*. For the imaging *in situ*, the intraoperative guidance is also important for tumor resection to prevent cancer recurrence. The specific nanomaterials functionalized with ligands that could recognize cancer biomarkers are widely applied to SERS and FLI[245,246] for intraoperative diagnosis. LIBS mapping is also a potential for cancer intradiagnosis. LIBS spectra including information of tissues might instruct doctors to distinguish normal, adjacent, and cancerous tissues during surgery when they aren't sure. Thus, the algorithm of the discrimination model is critical.

The above-reviewed imaging systems in conjunction with traditional imaging techniques may exhibit neglected information from another angle and precise diagnosis. However, compared with present clinical imaging techniques, the reviewed spectroscopic techniques complete *in vivo* imaging rarely particularly in a nontraumatic way except the integration with nanomaterials. More importantly, these nanomaterials with metal components (i.e., Fe, Mn, or Cd, etc.) could be integrated with conventional imaging systems, such as MRI or CT, to enhance imaging depth and accuracy. Consequently, the laser spectroscopic imaging technology could be developed up as auxiliary methods for clinical diagnosis due to the multimodal nanomaterial imaging contrast agents.

Acknowledgments

The authors are grateful for financial support from the Sichuan Science and Technology Program (2019ZDZX0036), and the support from the Analytical & Testing Center of Sichuan University.

Conflict of Interest

The authors declare no conflict of interest.

Supporting Information

The material is available at https://www.worldscientific.com/doi/suppl/10.1142/S1793545823300082

References

1. H. Sung, J. Ferlay, R. L. Siegel, M. Laversanne, I. Soerjomataram, A. Jemal, F. Bray, *CA: Cancer J. Clin.* **71**, 209–249 (2021).
2. S. Kunjachan, J. Ehling, G. Storm, F. Kiessling, T. Lammers, *Chem. Rev.* **115**, 10907–10937 (2015).
3. *Drug Ther. Bull.***49**, 141–144 (2011).
4. D. W. Townsend, *Semin. Nucl. Med.* **38**, 152–166 (2008).
5. W. A. Gibby, *Neurosurg. Clin. N. Am.* **16**, 1–64 (2005).
6. D. L. Gerrard, H. J. Bowley, *Anal. Chem.* **60**, 368–377 (1988).
7. C. L. Putzig, M. A. Leugers, M. L. McKelvy, G. E. Mitchell, R. A. Nyquist, R. R. Papenfuss, L. Yurga, *Anal. Chem.* **66**, 26–66 (1994).
8. A. Rosencwaig, *Annu. Rev. Biophys. Bioeng.* **9**, 31–54 (1980).
9. K. Y. Yamamoto, D. A. Cremers, L. E. Foster, M. P. Davies, R. D. Harris, *Appl. Spectrosc.* **59**, 1082–1097 (2005).
10. R. B. Sekar, A. Periasamy*J. Cell Biol.* **160**, 629–633 (2003).
11. S. K. Nune, P. Gunda, P. K. Thallapally, Y. Y. Lin, M. L. Forrest, C. J. Berkland, *Expert Opin. Drug Deliv.* **6**, 1175–1194 (2009).
12. H. Maeda, H. Nakamura, J. Fang, *Adv. Drug Deliv. Rev.* **65**, 71–79 (2013).
13. H.-H. Han, H.-M. Wang, P. Jangili, M. Li, L. Wu, Y. Zang, A. C. Sedgwick, J. Li, X.-P. He, T. D. James, J. S. Kim, *Chem. Soc. Rev.* **52**, 879–920 (2023).
14. C. Lai, B. Zhang, D. Li, X. Tan, B. Luo, J. Shen, L. Li, J. Shao, *J. Colloid Interface Sci.* **635**, 441–455 (2023).
15. Y. Yu, H. Jia, Y. Liu, L. Zhang, G. Feng, B. Z. Tang, *Molecules* **28**, 332 (2023).
16. N. C. Lindquist, C. D. L. D. Albuquerque, R. G. Sobral-Filho, I. Paci, A. G. Brolo, *Nat. Nanotechnol.* **14**, 981–987 (2019).
17. R. A. Harder, L. A. Wijenayaka, H. T. Phan, A. J. Haes, *J. Raman Spectrosc.* **52**, 497–505 (2021).
18. J. L. Johnson, M. Merrilees, J. Shragge, K. V. Wijk, *Photoacoustics* **9**, 62–72 (2018).
19. G. Xu, Z.-X. Meng, J.-D. Lin, C. X. Deng, P. L. Carson, J. B. Fowlkes, C. Tao, X. Liu, X. Wang, *Sci. Rep.* **6**, 16937 (2016).
20. J. Hui, R. Li, E. H. Phillips, C. J. Goergen, M. Sturek, J. X. Cheng, *Photoacoustics* **4**, 11–21 (2016).
21. S. Zhu, R. Tian, A. L. Antaris, X. Chen, H. Dai, *Adv. Mater.*1900321 (2019), doi: 10.1002/adma.201900321.
22. S. Luo, E. Zhang, Y. Su, T. Cheng, C. Shi, *Biomaterials* **32**, 7127–7138 (2011).
23. V. K. Singh, A. K. Rai, *Lasers Med. Sci.* **26**, 673–687 (2011).

24. L. K. Rotter, N. Berisha, H. T. Hsu, K. H. Burns, C. Andreou, M. F. Kircher, *Nanotheranostics* **6**, 256–269 (2022).
25. C. Andreou, V. Neuschmelting, D. F. Tschaharganeh, C. H. Huang, A. Oseledchyk, P. Iacono, H. Karabeber, R. R. Colen, L. Mannelli, S. W. Lowe, M. F. Kircher, *ACS Nano* **10**, 5015–5026 (2016).
26. P. Yin, B. Hu, Q. Li, Y. Duan, Q. Lin, *IEEE Trans. Instrum. Measure.* **70**, 1–7 (2021).
27. G. W. Auner, S. K. Koya, C. Huang, B. Broadbent, M. Trexler, Z. Auner, A. Elias, K. C. Mehne, M. A. Brusatori, *Cancer Metastasis Rev.* **37**, 691–717 (2018).
28. W. J. Tipping, M. Lee, A. Serrels, V. G. Brunton, A. N. Hulme, *Chem. Soc. Rev.* **45**, 2075–2089 (2016).
29. S. Cui, S. Zhang, S. Yue, *J. Healthc. Eng.* **2018**, 8619342 (2018).
30. S. You, H. Tu, Y. Zhao, Y. Liu, E. J. Chaney, M. Marjanovic, S. A. Boppart, *Sci. Rep.* **6**, 32922–32922 (2016).
31. J. N. Bentley, M. Ji, X. S. Xie, D. A. Orringer, *Expert Rev. Anticancer Ther.* **14**, 359–361 (2014).
32. X. Zhang, M. B. J. Roeffaers, S. Basu, J. R. Daniele, D. Fu, C. W. Freudiger, G. R. Holtom, X. S. Xie, *Chem Phys Chem* **13**, 1054–1059 (2012).
33. S. Keren, C. Zavaleta, Z. Cheng, A. D. L. Zerda, O. Gheysens, S. S. Gambhir, *Proc. Natl. Acad. Sci. USA* **105**, 5844–5849 (2008).
34. C. Zavaleta, A. D. L. Zerda, Z. Liu, S. Keren, Z. Cheng, M. Schipper, X. Chen, H. Dai, S. S. Gambhir, *Nano Lett.* **8**, 2800–2805 (2008).
35. H. Wei, H. Xu, *Nanoscale* **5**, 10794–10805 (2013).
36. P. L. Stiles, J. A. Dieringer, N. C. Shah, R. P. V. Duyne, *Annu. Rev. Anal. Chem.* **1**, 601–626 (2008).
37. L. A. Lane, X. Qian, S. Nie, *Chem. Rev.* **115**, 10489–10529 (2015).
38. M. Rycenga, C. M. Cobley, J. Zeng, W. Li, C. H. Moran, Q. Zhang, D. Qin, Y. Xia, *Chem. Rev.* **111**, 3669–3712 (2011).
39. J. M. Nam, J. W. Oh, H. Lee, Y. D. Suh, *Acc. Chem. Res.* **49**, 2746–2755 (2016).
40. E. Lenzi, D. J. D. Aberasturi, L. M. Liz-Marzán, *ACS Sens.* **4**, 1126–1137 (2019).
41. N. G. Khlebtsov, L. Lin, B. N. Khlebtsov, J. Ye, *Theranostics* **10**, 2067–2094 (2020).
42. J. L. Campbell, E. D. SoRelle, O. Ilovich, O. Liba, M. L. James, Z. Qiu, V. Perez, C. T. Chan, A. D. L. Zerda, C. Zavaleta, *Biomaterials* **135**, 42–52 (2017).
43. R. McQueenie, R. Stevenson, R. Benson, N. MacRitchie, I. McInnes, P. Maffia, K. Faulds, D. Graham, J. Brewer, P. Garside, *Anal. Chem.* **84**, 5968–5975 (2012).
44. S. E. J. Bell, G. Charron, E. Cortés, J. Kneipp, M. L. D. L. Chapelle, J. Langer, M. Procházka, V. Tran, S. Schlücker, *Angew. Chem. Int. Ed.* **59**, 5454–5462 (2020).
45. C. Duffield, N. Lyu, Y. Wang, *J. Innov. Opt. Health Sci.* **14**, 2141007 (2021).
46. Y. Chen, J.-Q. Ren, X.-G. Zhang, D.-Y. Wu, A.-G. Shen, J.-M. Hu, *Anal. Chem.* **88**, 6115–6119 (2016).
47. Y. Su, S. Wen, X. Luo, F. Xue, S. Wu, B. Yuan, X. Lu, C. Cai, L.-P. Jiang, P. Wu, J.-J. Zhu, *ACS Appl. Mater. Interfaces* **13**, 135–147 (2021).
48. F. Deiss, N. Sojic, D. J. White, P. R. Stoddart, *Anal. Bioanal. Chem.* **396**, 53–71 (2010).
49. S. Lee, J. Kim, H. Yang, E. Cortés, S. Kang, S. W. Han, *Angew. Chem. Int. Ed.* **58**, 15890–15894 (2019).
50. Y. Liu, J. R. Ashton, E. J. Moding, H. Yuan, J. K. Register, A. M. Fales, J. Choi, M. J. Whitley, X. Zhao, Y. Qi, Y. Ma, G. Vaidyanathan, M. R. Zalutsky, D. G. Kirsch, C. T. Badea, T. Vo-Dinh, *Theranostics* **5**, 946–960 (2015).
51. F. Tian, J. Conde, C. Bao, Y. Chen, J. Curtin, D. Cui, *Biomaterials* **106**, 87–97 (2016).
52. L. Zeng, Y. Pan, S. Wang, X. Wang, X. Zhao, W. Ren, G. Lu, A. Wu, *ACS Appl. Mater. Interfaces* **7**, 16781–16791 (2015).
53. T. R. Nayak, C. Andreou, A. Oseledchyk, W. D. Marcus, H. C. Wong, J. Massagué, M. F. Kircher, *Nanoscale* **9**, 1110–1119 (2017).
54. L. Jiang, J. Qian, F. Cai, S. He, *Anal. Bioanal. Chem.* **400**, 2793 (2011).
55. C. Wen, H. Chen, X. Guo, Z. Lin, S. Zhang, X.-C. Shen, H. Liang, *Langmuir* **37**, 569–577 (2021).
56. N. Yan, X. Wang, L. Lin, T. Song, P. Sun, H. Tian, H. Liang, X. Chen, *Adv. Funct. Mater.* **28**, 1800490 (2018).
57. J. V. Jokerst, A. J. Cole, D. V. D. Sompel, S. S. Gambhir, *ACS Nano* **6**, 10366–10377 (2012).
58. J. Yue, Z. Liu, X. Cai, X. Ding, S. Chen, K. Tao, T. Zhao, *Talanta* **150**, 503–509 (2016).
59. Z. A. Nima, M. Mahmood, Y. Xu, T. Mustafa, F. Watanabe, D. A. Nedosekin, M. A. Juratli, T. Fahmi, E. I. Galanzha, J. P. Nolan, A. G. Basnakian, V. P. Zharov, A. S. Biris, *Sci. Rep.* **4** (2015).
60. Z. Wang, S. Zong, J. Yang, J. Li, Y. Cui, *Biosens. Bioelectron.* **26**, 2883–2889 (2011).
61. Y. Zhang, J. Qian, D. Wang, Y. Wang, S. He, *Angew. Chem. Int. Ed.* **52**, 1148–1151 (2013).
62. S. Lal, S. Link, N. J. Halas, *Nat. Photonics* **1**, 641–648 (2007).

63. J. He, Q. Wei, S. Wang, S. Hua, M. Zhou, *Biomaterials* **271**, 120734 (2021).
64. Y. Qiu, M. Lin, G. Chen, C. Fan, M. Li, X. Gu, S. Cong, Z. Zhao, L. Fu, X. Fang, Z. Xiao, *ACS Appl. Mater. Interfaces* **11**, 23436–23444 (2019).
65. Q. Lv, M.-Y. Gao, Z.-H. Cheng, Q. Chen, A.-G. Shen, J.-M. Hu, *Chem. Commun.* **54**, 13399–13402 (2018).
66. K. L. Wustholz, C. L. Brosseau, F. Casadio, R. P. V. Duyne, *Phys. Chem. Chem. Phys.* **11**, 7350 (2009).
67. A. Samanta, K. K. Maiti, K.-S. Soh, X. Liao, M. Vendrell, U. S. Dinish, S.-W. Yun, R. Bhuvaneswari, H. Kim, S. Rautela, J. Chung, M. Olivo, Y.-T. Chang, *Angew. Chem. Int. Ed.* **50**, 6089–6092 (2011).
68. M. Spaliviero, S. Harmsen, R. Huang, M. A. Wall, C. Andreou, J. A. Eastham, K. A. Touijer, P. T. Scardino, M. F. Kircher, *Mol. Imaging Biol.* **18**, 677–685 (2016).
69. J. H. Yu, I. Steinberg, R. M. Davis, A. V. Malkovskiy, A. Zlitni, R. K. Radzyminski, K. O. Jung, D. T. Chung, L. D. Curet, A. L. D'Souza, E. Chang, J. Rosenberg, J. Campbell, H. Frostig, S. M. Park, G. Pratx, C. Levin, S. S. Gambhir, *ACS Nano* **15**, 19956–19969 (2021).
70. F. Nicolson, B. Andreiuk, C. Andreou, H. T. Hsu, S. Rudder, M. F. Kircher, *Theranostics* **9**, 5899–5913 (2019).
71. M. E. Berry, S. M. McCabe, S. Sloan-Dennison, S. Laing, N. C. Shand, D. Graham, K. Faulds, *ACS Appl. Mater. Interfaces* (2022), doi: 10.1021/acsami.2c05611.
72. Y. Zhang, L. Lin, J. He, J. Ye, *J. Innov. Opt. Health Sci.* **14**, 2141001 (2021).
73. S. L. Jacques, *Appl. Opt.* **32**, 2447–2454 (1993).
74. J. Yao, L. V. Wang, *Laser Photonics Rev.* **7**, 758–778 (2013).
75. R. I. Siphanto, K. K. Thumma, R. G. M. Kolkman, T. G. V. Leeuwen, F. F. M. D. Mul, J. W. V. Neck, L. N. A. V. Adrichem, W. Steenbergen, *Opt. Express* **13**, 89–95 (2005).
76. B. Ning, M. J. Kennedy, A. J. Dixon, N. Sun, R. Cao, B. T. Soetikno, R. Chen, Q. Zhou, K. K. Shung, J. A. Hossack, S. Hu, *Opt. Lett.* **40**, 910–913 (2015).
77. G. Huang, J. Lv, Y. He, J. Yang, L. Zeng, L. Nie, *Photoacoustics* **28**, 100410 (2022).
78. R. Cao, J. Li, B. Ning, N. Sun, T. Wang, Z. Zuo, S. Hu, *NeuroImage* **150**, 77–87 (2017).
79. L. V. Wang, *Med. Phys.* **35**, 5758–5767 (2008).
80. L. V. Wang, *Nat. Photonics* **3**, 503–509 (2009).
81. J.-M. Yang, K. Maslov, H.-C. Yang, Q. Zhou, K. K. Shung, L. V. Wang, *Opt. Lett.* **34**, 1591–1593 (2009).
82. Y. Zheng, M. Liu, L. Jiang, *Front. Chem.* **10** (2022).
83. D. Biswas, S. Roy, S. Vasudevan, *Micromachines* **13**, 1900 (2022).
84. A. Danielli, K. Maslov, C. P. Favazza, J. Xia, L. V. Wang, *Appl. Phys. Lett.* **106**, 203701–203701 (2015).
85. G. Ara, R. R. Anderson, K. G. Mandel, M. Ottesen, A. R. Oseroff, *Lasers Surg. Med.* **10**, 52–59 (1990).
86. P. Spencer, J. M. Payne, C. M. Cobb, L. Reinisch, G. M. Peavy, D. D. Drummer, D. L. Suchman, J. R. Swafford, *J. Periodontol.* **70**, 68–74 (1999).
87. H.-W. Wang, N. Chai, P. Wang, S. Hu, W. Dou, D. Umulis, L. V. Wang, M. Sturek, R. Lucht, J.-X. Cheng, *Phys. Rev. Lett.* **106**, 238106–238106 (2011).
88. D. Wu, L. Huang, M. S. Jiang, H. Jiang, *Int. J. Mol. Sci.* **15**, 23616–23639 (2014).
89. Y. Tian, S. Qiang, L. Wang, *Front. Bioeng. Biotechnol.* **7** (2019).
90. V. P. Nguyen, Y. Li, W. Qian, B. Liu, C. Tian, W. Zhang, Z. Huang, A. Ponduri, M. Tarnowski, X. Wang, Y. M. Paulus, *Sci. Rep.* **9**, 5945 (2019).
91. C. Du, L. Zhou, J. Qian, M. He, C. M. Dong, J. D. Xia, Z. G. Zhang, R. Zhang, *J. Mater. Chem. B* **9**, 5484–5491 (2021).
92. Y. Xia, W. Li, C. M. Cobley, J. Chen, X. Xia, Q. Zhang, M. Yang, E. C. Cho, P. K. Brown, *Acc. Chem. Res.* **44**, 914–924 (2011).
93. M. Yang, J. Li, P. Gu, X. Fan, *Bioact. Mater.* **6**, 1973–1987 (2021).
94. C. Liu, S. Li, Y. Gu, H. Xiong, W. T. Wong, L. Sun, *Mol. Imaging Biol.* **20**, 919–929 (2018).
95. S. M. Mousavi, M. Zarei, S. A. Hashemi, S. Ramakrishna, W.-H. Chiang, C. W. Lai, A. Gholami, *Drug Metab. Rev.* **52**, 299–318 (2020).
96. A. D'Hollander, G. V. Velde, H. Jans, B. Vanspauwen, E. Vermeersch, J. Jose, T. Struys, T. Stakenborg, L. Lagae, U. Himmelreich, *Nanomaterials (Basel)* **10** (2020).
97. P. Ning, Y. Chen, Q. Bai, C. Xu, C. Deng, Q. Cheng, Y. Cheng, *ACS Appl. Mater. Interfaces* **14**, 7551–7564 (2022).
98. C. J. Murphy, T. K. Sau, A. M. Gole, C. J. Orendorff, J. Gao, L. Gou, S. E. Hunyadi, T. Li, *J. Phys. Chem. B* **109**, 13857–13870 (2005).
99. Y. Zhao, F. Ye, T. B. Brismar, X. Li, R. He, R. Heuchel, R. El-Sayed, N. Feliu, W. Zheng, S. Oerther, J. Dutta, W. J. Parak, M. Muhammed, M. Hassan, *ACS Appl. Mater. Interfaces* (2020), doi: 10.1021/acsami.0c15430.

100. J. Pérez-Juste, I. Pastoriza-Santos, L. M. Liz-Marzán, P. Mulvaney, *Coord. Chem. Rev.* **249**, 1870–1901 (2005).
101. B. J. Tromberg, N. Shah, R. Lanning, A. Cerussi, J. Espinoza, T. Pham, L. Svaasand, J. Butler, *Neoplasia* **2**, 26–40 (2000).
102. P. Li, Y. Wu, D. Li, X. Su, C. Luo, Y. Wang, J. Hu, G. Li, H. Jiang, W. Zhang, *uNanoscale Res. Lett.* **13** (2018).
103. Y.-S. Chen, Y. Zhao, S. J. Yoon, S. S. Gambhir, S. Emelianov, *Nat. Nanotechnol.* **14**, 465–472 (2019).
104. K. Cai, W. Zhang, M. F. Foda, X. Li, J. Zhang, Y. Zhong, H. Liang, H. Li, H. Han, T. Zhai, *Small* **16**, 2002748 (2020).
105. F. Gao, L. Bai, S. Liu, R. Zhang, J. Zhang, X. Feng, Y. Zheng, Y. Zhao, *Nanoscale* **9**, 79–86 (2017).
106. R. K. Hartman, K. A. Hallam, E. M. Donnelly, S. Y. Emelianov, *Laser Phys. Lett.* **16**, 025603 (2019).
107. K. J. McHugh, L. Jing, A. M. Behrens, S. Jayawardena, W. Tang, M. Gao, R. Langer, A. Jaklenec, *Adv. Mater.* **30**, 1706356 (2018).
108. Y. T. Lim, S. Kim, A. Nakayama, N. E. Stott, M. G. Bawendi, J. V. Frangioni, *Mol. Imaging* **2**, 50–64 (2003), doi: 10.1162/15353500200302163.
109. J. Cui, R. Jiang, S. Xu, G. Hu, L. Wang, *Small* **11**, 4183–4190 (2015).
110. L. Cheng, J. Liu, X. Gu, H. Gong, X. Shi, T. Liu, C. Wang, X. Wang, G. Liu, H. Xing, W. Bu, B. Sun, Z. Liu, *Adv. Mater.* **26**, 1886–1893 (2014).
111. W. Yin, L. Yan, J. Yu, G. Tian, L. Zhou, X. Zheng, X. Zhang, Y. Yong, J. Li, Z. Gu, Y. Zhao, *ACS Nano* **8**, 6922–6933 (2014).
112. S. Wang, J. Lin, T. Wang, X. Chen, P. Huang, *Theranostics* **6**, 2394–2413 (2016).
113. K. Yang, G. Yang, L. Chen, L. Cheng, L. Wang, C. Ge, Z. Liu, *Biomaterials* **38**, 1–9 (2015).
114. A. Li, X. Li, X. Yu, W. Li, R. Zhao, X. An, D. Cui, X. Chen, W. Li, *Biomaterials* **112**, 164–175 (2017).
115. Z. Wang, P. Huang, O. Jacobson, Z. Wang, Y. Liu, L. Lin, J. Lin, N. Lu, H. Zhang, R. Tian, G. Niu, G. Liu, X. Chen, *ACS Nano* **10**, 3453–3460 (2016).
116. H. Zhang, T. Wang, H. Liu, F. Ren, W. Qiu, Q. Sun, F. Yan, H. Zheng, Z. Li, M. Gao, *Nanoscale* **11**, 7600–7608 (2019).
117. C. G. Liu, H. X. Tang, X. Zheng, D. Y. Yang, Y. Zhang, J. T. Zhang, R. K. Kankala, S. B. Wang, G. Liu, A. Z. Chen, *ACS Appl. Mater. Interfaces* **12**, 40673–40683 (2020).
118. L. J. Rich, J. A. Damasco, J. C. Bulmahn, H. L. Kutscher, P. N. Prasad, M. Seshadri, *Cancers (Basel)* **12** (2020).
119. L. Chen, J. Chen, S. Qiu, L. Wen, Y. Wu, Y. Hou, Y. Wang, J. Zeng, Y. Feng, Z. Li, H. Shan, M. Gao, *Small* **14** (2018).
120. K. Zhang, Z. Yang, X. Meng, Y. Cao, Y. Zhang, W. Dai, H. Lu, Z. Yu, H. Dong, X. Zhang, *Mater. Chem. Front.* **2**, 1184–1194 (2018).
121. Y. Duan, Y. Xu, D. Mao, W. H. Liew, B. Guo, S. Wang, X. Cai, N. Thakor, K. Yao, C. J. Zhang, B. Liu, *Small* **14**, e1800652 (2018).
122. X.-R. Song, S.-X. Yu, G.-X. Jin, X. Wang, J. Chen, J. Li, G. Liu, H.-H. Yang, *Small* **12**, 1506–1513 (2016).
123. T. T. V. Phan, N. Q. Bui, M. S. Moorthy, K. D. Lee, J. Oh, *Nanoscale Res. Lett.* **12**, 570 (2017).
124. Y. Zhang, Q. Shen, Q. Li, P. He, J. Li, F. Huang, J. Wang, Y. Duan, C. Shen, F. Saleem, Z. Luo, L. Wang, *Adv. Sci.* **8**, e2100386 (2021).
125. W. Tao, X. Ji, X. Zhu, L. Li, J. Wang, Y. Zhang, P. E. Saw, W. Li, N. Kong, M. A. Islam, T. Gan, X. Zeng, H. Zhang, M. Mahmoudi, G. J. Tearney, O. C. Farokhzad, *Adv. Mater.* **30**, 1802061 (2018).
126. J. Yu, X. H. Wang, J. Feng, X. Meng, X. Bu, Y. Li, N. Zhang, P. Wang, *Adv. Healthc. Mater.* **8**, e1900378 (2019).
127. X. Jin, C. Xu, J. Hu, S. Yao, Z. Hu, B. Wang, *J. Mater. Chem. B* **9**, 9333–9346 (2021).
128. J. Lin, X. Chen, P. Huang, *Adv. Drug Deliv. Rev.* **105**, 242–254 (2016).
129. H. Ding, Y. Cai, L. Gao, M. Liang, B. Miao, H. Wu, Y. Liu, N. Xie, A. Tang, K. Fan, X. Yan, G. Nie, *Nano Lett.* **19**, 203–209 (2019).
130. Y. Xuan, R.-Y. Zhang, D.-H. Zhao, X.-S. Zhang, J. An, K. Cheng, X.-L. Hou, X.-L. Song, Y.-D. Zhao, X.-Q. Yang, *Chem. Eng. J.* **369**, 87–99 (2019).
131. R. K. Vayalakkara, C.-L. Lo, H.-H. Chen, M.-Y. Shen, Y.-C. Yang, A. Sabu, Y.-F. Huang, H.-C. Chiu, *J. Control. Release* **345**, 417–432 (2022).
132. M. Guan, Y. Xuan, Y. Gao, Y. Liu, S. Zhang, *J. Mater. Sci.* **57**, 7056–7067 (2022).
133. Q. Li, K. Chen, W. Huang, H. Ma, X. Zhao, J. Zhang, Y. Zhang, C. Fang, L. Nie, *Cancer Lett.* **496**, 169–178 (2021).
134. J. Zhao, F. Gong, N. Yang, H. Lei, Z. Han, Y. Yang, L. Cheng, *J. Innov. Opt. Health Sci.* **15**, 2250026 (2022).
135. L. Nie, D. Xing, S. Yang, *Med. Phys.* **36**, 3429–3437 (2009).
136. Z. Qin, Y. Liu, J. Chi, Y. Ma, M. Sun, *J. Innov. Opt. Health Sci.* **15**, 2250030 (2022).

137. E. Vienneau, W. Liu, J. Yao, *Opt. Lett.* **43**, 4413–4416 (2018).
138. C. Wang, Y.-F. Lu, C.-M. Cai, H.-Z. Xiang, G. Zheng, *World J. Gastroenterol.* **24**, 3531–3537 (2018).
139. M. Mozaffarzadeh, M. H. H. Varnosfaderani, A. Sharma, M. Pramanik, N. D. Jong, M. D. Verweij, *J. Biophotonics* **12**, e201900133 (2019).
140. Q. Zhao, R. Lin, C. Liu, J. Zhao, G. Si, L. Song, J. Meng, *J. Biophotonics* **12**, e201800421 (2019).
141. S. Alshahrani, Y. Yan, I. Avrutsky, M. Anastasio, E. Malyarenko, N. Duric, M. Mehrmohammadi, "Design and development of a full-ring ultrasound and photoacoustic tomography system for breast cancer imaging," (2017).
142. Y. Zhang, L. Wang, *IEEE Trans. Med. Imaging* **39**, 4369–4375 (2020).
143. H. C. Ishikawa-Ankerhold, R. Ankerhold, G. P. C. Drummen, *Molecules* **17**, 4047–4132 (2012).
144. A. Seifalian, S. Rizvi, S. Rouhi, S. Taniguchi, S. Y. Yang, M. Green, M. Keshtgar, *Int. J. Nanomed.* 1323 (2014), doi: 10.2147/ijn.s51535.
145. M. E. T. Carvalho, W. F. Oliveira, C. R. A. Cunha, L. C. B. B. Coelho, M. V. Silva, L. B. CarvalhoJr., B. S. Santos, P. E. C. Filho, A. Fontes, M. T. S. Correia, *Int. J. Biol. Macromol.* **138**, 302–308 (2019).
146. K. Hu, H. Wang, G. Tang, T. Huang, X. Tang, X. Liang, S. Yao, D. Nie, *J. Nucl. Med.* **56**, 1278–1284 (2015).
147. X. Gao, Y. Cui, R. M. Levenson, L. W. K. Chung, S. Nie, *Nat. Biotechnol.* **22**, 969–976 (2004).
148. J. S. Kim, K. J. Cho, T. H. Tran, M. Nurunnabi, T. H. Moon, S. M. Hong, Y. K. Lee, *J. Colloid Interface Sci.* **353**, 363–371 (2011).
149. L. Trapiella-Alfonso, T. Pons, N. Lequeux, L. Leleu, J. Grimaldi, M. Tasso, E. Oujagir, J. Seguin, F. D'Orlyé, C. Girard, B.-T. Doan, A. Varenne, *ACS Appl. Mater. Interfaces* **10**, 17107–17116 (2018).
150. W. Wang, H. Mattoussi, *Acc. Chem. Res.* **53**, 1124–1138 (2020).
151. M. Shi, L. Dong, S. Zheng, P. Hou, L. Cai, M. Zhao, X. Zhang, Q. Wang, J. Li, K. Xu, *Biochem. Biophys. Res. Commun.* **516**, 1090–1096 (2019).
152. J. Kwon, S. W. Jun, S. I. Choi, X. Mao, J. Kim, E. K. Koh, Y.-H. Kim, S.-K. Kim, D. Y. Hwang, C.-S. Kim, J. Lee, *Sci. Adv.* **5**, eaay0044 (2019).
153. X. L. Ge, B. Huang, Z. L. Zhang, X. Liu, M. He, Z. Yu, B. Hu, R. Cui, X. J. Liang, D. W. Pang, *J. Mater. Chem. B* **7**, 5782–5788 (2019).
154. J. J. Zhang, Y. Lin, H. Zhou, H. He, J. J. Ma, M. Y. Luo, Z. L. Zhang, D. W. Pang, *Adv. Healthc. Mater.* **8**, e1900341 (2019).
155. J. Zhang, G. Hao, C. Yao, J. Yu, J. Wang, W. Yang, C. Hu, B. Zhang, *ACS Appl. Mater. Interfaces* **8**, 16612–16621 (2016).
156. N. Liu, M. Tang, *J. Hazard. Mater.* **399**, 122606 (2020).
157. S. Li, Z. Guo, Y. Zhang, W. Xue, Z. Liu, *ACS Appl. Mater. Interfaces* **7**, 19153–19162 (2015).
158. H. Groß, J. M. Hamm, T. Tufarelli, O. Hess, B. Hecht, *Sci. Adv.* **4**, eaar4906 (2018).
159. J. Liao, Y. Yao, C. H. Lee, Y. Wu, P. Li, *Pharmaceutics* **13** (2021).
160. X. W. Hua, Y. W. Bao, J. Zeng, F. G. Wu, *ACS Appl. Mater. Interfaces* **11**, 32647–32658 (2019).
161. X. Bao, Y. Yuan, J. Chen, B. Zhang, D. Li, D. Zhou, P. Jing, G. Xu, Y. Wang, K. Hola, D. Shen, C. Wu, L. Song, C. Liu, R. Zboril, S. Qu, *Light Sci. Appl.* **7**, 91 (2018).
162. Y. Su, S. Liu, Y. Guan, Z. Xie, M. Zheng, X. Jing, *Biomaterials* **255**, 120110 (2020).
163. B. B. Karakoçak, A. Laradji, T. Primeau, M. Y. Berezin, S. Li, N. Ravi, *ACS Appl. Mater. Interfaces* **13**, 277–286 (2021).
164. S. Wang, L. Chen, J. Wang, J. Du, Q. Li, Y. Gao, S. Yu, Y. Yang, *Mater. Sci. Eng. C, Mater. Biol. Appl.* **116**, 111233 (2020).
165. H. Liu, X. Lv, J. Qian, H. Li, Y. Qian, X. Wang, X. Meng, W. Lin, H. Wang, *ACS Nano* **14**, 13304–13315 (2020).
166. H. Liu, C. Li, Y. Qian, L. Hu, J. Fang, W. Tong, R. Nie, Q. Chen, H. Wang, *Biomaterials* **232**, 119700 (2020).
167. H. Zhang, S. Ba, Z. Yang, T. Wang, J. Y. Lee, T. Li, F. Shao, *ACS Appl. Mater. Interfaces* **12**, 13634–13643 (2020).
168. X.-W. Hua, Y.-W. Bao, J. Zeng, F.-G. Wu, *ACS Appl. Mater. Interfaces* **11**, 32647–32658 (2019).
169. Y. Liu, J. Liu, J. Zhang, X. Li, F. Lin, N. Zhou, B. Yang, L. Lu, *ACS Omega* **3**, 7888–7896 (2018).
170. D. M. Wu, A. García-Etxarri, A. Salleo, J. A. Dionne, *J. Phys. Chem. Lett.* **5**, 4020–4031 (2014).
171. W. Park, D. Lu, S. Ahn, *Chem. Soc. Rev.* **44**, 2940–2962 (2015).
172. K. L. Reddy, R. Balaji, A. Kumar, V. Krishnan, *Small* **14**, 1801304 (2018).
173. J. Zhou, Z. Liu, F. Li, *Chem. Soc. Rev.* **41**, 1323–1349 (2012).
174. Q. Liu, M. Chen, Y. Sun, G. Chen, T. Yang, Y. Gao, X. Zhang, F. Li, *Biomaterials* **32**, 8243–8253 (2011).
175. R. Wang, H. Yang, R. Fu, Y. Su, X. Lin, X. Jin, W. Du, X. Shan, G. Huang, *Cancers* **12**, 3136 (2020).

176. H. He, C. B. Howard, Y. Chen, S. Wen, G. Lin, J. Zhou, K. J. Thurecht, D. Jin, *Anal. Chem.* **90**, 3024–3029 (2018).
177. J. X. Cao, L. Zhang, X. Ding, D. Liu, B. Su, J. Y. Shi, *Small Methods* **4**, 9 (2020).
178. W. Zhang, B. Peng, F. Tian, W. Qin, X. Qian, *Anal. Chem.* **86**, 482–489 (2014).
179. Y. Han, Y. An, G. Jia, X. Wang, C. He, Y. Ding, Q. Tang, *Nanoscale* **10**, 6511–6523 (2018).
180. S. Yu, D. Jang, H. Yuan, W.-T. Huang, M. Kim, F. M. Mota, R.-S. Liu, H. Lee, S. Kim, D. H. Kim, *ACS Appl. Mater. Interfaces* **13**, 58422–58433 (2021).
181. J. Zhou, P. Luo, C. Sun, L. Meng, W. Ye, S. Chen, B. Du, *Nanoscale* **9**, 4244–4254 (2017).
182. J. Jin, Z. Xu, Y. Zhang, Y. J. Gu, M. H. Lam, W. T. Wong, *Adv. Healthc. Mater.* **2**, 1501–1512 (2013).
183. J. Lee, A. C. Gordon, H. Kim, W. Park, S. Cho, B. Lee, A. C. Larson, E. A. Rozhkova, D. H. Kim, *Biomaterials* **109**, 69–77 (2016).
184. J. Chen, D. Zhang, Y. Zou, Z. Wang, M. Hao, M. Zheng, X. Xue, X. Pan, Y. Lu, J. Wang, B. Shi, *J. Mater. Chem. B* **6**, 7862–7870 (2018).
185. W.-T. Huang, M.-H. Chan, X. Chen, M. Hsiao, R.-S. Liu, *Theranostics* **10**, 782–796 (2020).
186. M.-H. Chan, Y.-T. Pan, Y.-C. Chan, M. Hsiao, C.-H. Chen, L. Sun, R.-S. Liu, *Chem. Sci.* **9**, 3141–3151 (2018).
187. Y. Ji, F. Lu, W. Hu, H. Zhao, Y. Tang, B. Li, X. Hu, X. Li, X. Lu, Q. Fan, W. Huang, *Biomaterials* **219**, 119393 (2019).
188. H. B. Cheng, Y. Li, B. Z. Tang, J. Yoon, *Chem. Soc. Rev.* **49**, 21–31 (2020).
189. D. Svechkarev, A. M. Mohs, *Curr. Med. Chem.* **26**, 4042–4064 (2019).
190. K. Ilina, W. M. MacCuaig, M. Laramie, J. N. Jeouty, L. R. McNally, M. Henary, *Bioconjug. Chem.* **31**, 194–213 (2020).
191. C. Schierl, W. Alex, L. M. Mateo, B. Ballesteros, D. Shimizu, A. Osuka, T. Torres, D. M. Guldi, G. Bottari, *Angew. Chem. Int. Ed.* **58**, 14644–14652 (2019).
192. Z. Shi, X. Han, W. Hu, H. Bai, B. Peng, L. Ji, Q. Fan, L. Li, W. Huang, *Chem. Soc. Rev.* **49**, 7533–7567 (2020).
193. L. Guo, B. Xu, H. Chen, Y. Tang, *J. Innov. Opt. Health Sci.* **15**, 2240007 (2022).
194. Y. Zhou, W. Zeng, M. Wang, R. Li, X. Yue, Z. Dai, *J. Innov. Opt. Health Sci.* **15**, 2250035 (2022).
195. H. Li, M. Wei, X. Lv, Y. Hu, J. Shao, X. Song, D. Yang, W. Wang, B. Li, X. Dong, *J. Innov. Opt. Health Sci.* **15**, 2230009 (2022).
196. Y. Zhang, G. Li, J. Li, M. Wu, X. Liu, J. Liu, *J. Innov. Opt. Health Sci.* **15**, 2240009 (2022).
197. H. Shi, Y. Lei, J. Ge, X. He, W. Cui, X. Ye, J. Liu, K. Wang, *Anal. Chem.* **91**, 9154–9160 (2019).
198. B. Wu, Y. Lin, B. Li, C. Zhan, F. Zeng, S. Wu, *Anal. Chem.* **90**, 9359–9365 (2018).
199. D. Gao, L. Gao, C. Zhang, H. Liu, B. Jia, Z. Zhu, F. Wang, Z. Liu, *Biomaterials* **53**, 229–238 (2015).
200. Q. Tang, Z. Cheng, N. Yang, Q. Li, P. Wang, D. Chen, W. Wang, X. Song, X. Dong, *Biomaterials* **205**, 1–10 (2019).
201. T. Ishizawa, N. Fukushima, J. Shibahara, K. Masuda, S. Tamura, T. Aoki, K. Hasegawa, Y. Beck, M. Fukayama, N. Kokudo, *Cancer* **115**, 2491–2504 (2009).
202. C. Zhang, T. Liu, Y. Su, S. Luo, Y. Zhu, X. Tan, S. Fan, L. Zhang, Y. Zhou, T. Cheng, C. Shi, *Biomaterials* **31**, 6612–6617 (2010).
203. Z. Yuan, L. Gui, J. Zheng, Y. Chen, S. Qu, Y. Shen, F. Wang, M. Er, Y. Gu, H. Chen, *ACS Appl. Mater. Interfaces* **10**, 30994–31007 (2018).
204. D. Zhang, Y.-X. Zhao, Z.-Y. Qiao, U. Mayerhöffer, P. Spenst, X.-J. Li, F. Würthner, H. Wang, *Bioconjug. Chem.* **25**, 2021–2029 (2014).
205. F.-P. Gao, Y.-X. Lin, L.-L. Li, Y. Liu, U. Mayerhöffer, P. Spenst, J.-G. Su, J.-Y. Li, F. Würthner, H. Wang, *Biomaterials* **35**, 1004–1014 (2014).
206. S. Sreejith, J. Joseph, M. Lin, N. V. Menon, P. Borah, H. J. Ng, Y. X. Loong, Y. Kang, S. W.-K. Yu, Y. Zhao, *ACS Nano* **9**, 5695–5704 (2015).
207. R. Li, K. Zheng, P. Hu, Z. Chen, S. Zhou, J. Chen, C. Yuan, S. Chen, W. Zheng, E. Ma, F. Zhang, J. Xue, X. Chen, M. Huang, *Theranostics* **4**, 642–659 (2014).
208. C. Zhang, L. Gao, Y. Cai, H. Liu, D. Gao, J. Lai, B. Jia, F. Wang, Z. Liu, *Biomaterials* **84**, 1–12 (2016).
209. F. Wang, Y. Zhu, L. Zhou, L. Pan, Z. Cui, Q. Fei, S. Luo, D. Pan, Q. Huang, R. Wang, C. Zhao, H. Tian, C. Fan, *Angew. Chem. Int. Ed.* **54**, 7349–7353 (2015).
210. W. Xiao, P. Wang, C. Ou, X. Huang, Y. Tang, M. Wu, W. Si, J. Shao, W. Huang, X. Dong, *Biomaterials* **183**, 1–9 (2018).
211. W. Lin, W. Zhang, S. Liu, Z. Li, X. Hu, Z. Xie, C. Duan, G. Han, *ACS Appl. Mater. Interfaces* **11**, 43928–43935 (2019).
212. J. P. Singh, J. R. Almirall, M. Sabsabi, A. W. Miziolek, *Anal. Bioanal. Chem.* **400**, 3191–3192 (2011).
213. F. J. Fortes, J. Moros, P. Lucena, L. M. Cabalín, J. J. Laserna, *Anal. Chem.* **85**, 640–669 (2013).
214. R. Noll, Material ablation, *Laser-Induced Breakdown Spectroscopy: Fundamentals and Applications*,

pp. 97–118, Springer, Berlin, Heidelberg (2012), doi: 10.1007/978-3-642-20668-9 _7.
215. R. Noll, Plasma dynamics and plasma parameters, *Laser-Induced Breakdown Spectroscopy: Fundamentals and Applications*, pp. 119–166, SpringerBerlin, Heidelberg (2012), doi: 10.1007/978-3-642-20668-9 _8.
216. R. Noll, Evaporation and plasma generation, *Laser-Induced Breakdown Spectroscopy: Fundamentals and Applications*, pp. 75–82, SpringerBerlin, Heidelberg (2012), doi: 10.1007/978-3-642-20668-9 _5.
217. M. Capitelli, G. Colonna, G. D'Ammando, R. Gaudiuso, L. D. Pietanza, Physical processes in optical emission spectroscopy, *Laser-Induced Breakdown Spectroscopy: Theory and Applications*, S. Musazzi, U. Perini, Eds., pp. 31–57, SpringerBerlin, Heidelberg (2014), doi: 10.1007/978-3-642-45085-3 _2.
218. V. K. Unnikrishnan, K. Alti, R. Nayak, R. Bernard, V. B. Kartha, C. Santhosh, G. P. Gupta, B. M. Suri, *Pramana* **75**, 1145–1150 (2010).
219. R. Kanawade, F. Mahari, F. Klämpfl, M. Rohde, C. Knipfer, K. Tangermann-Gerk, W. Adler, M. Schmidt, F. Stelzle, *J. Biophotonics* **8**, 153–161 (2015).
220. D. A. Cremers, L. J. Radziemski, T. R. Loree, *Appl. Spectrosc.* **38**, 721–729 (1984).
221. Y. Gimenez, B. Busser, F. Trichard, A. Kulesza, J. M. Laurent, V. Zaun, F. Lux, J. M. Benoit, G. Panczer, P. Dugourd, O. Tillement, F. Pelascini, L. Sancey, V. Motto-Ros, *Sci. Rep.* **6**, 29936 (2016).
222. V. K. Singh, V. Rai, A. K. Rai, *Lasers Med. Sci.* **24**, 27–33 (2009).
223. M. A. Gondal, R. K. Aldakheel, M. A. Almessiere, M. M. Nasr, J. A. Almusairii, B. Gondal, *J. Pharm. Biomed. Anal.* **183**, 10 (2020).
224. V. K. Singh, A. K. Rai, P. K. Rai, P. K. Jindal, *Lasers Med. Sci.* **24**, 749–759 (2009).
225. V. K. Singh, A. K. Rai, *Lasers Med. Sci.* **26**, 307–315 (2011).
226. S. Sasazawa, S. Kakino, Y. Matsuura, *J. Biomed. Opt.* **20**, 065002 (2015).
227. S. Moncayo, F. Trichard, B. Busser, M. Sabatier-Vincent, F. Pelascini, N. Pinel, I. Templier, J. Charles, L. Sancey, V. Motto-Ros, *Spectrochim. Acta B, At. Spectrosc.* **133**, 40–44 (2017).
228. Q. Lin, S. Wang, Y. Duan, V. V. Tuchin, *J. Biophotonics*e202000479 (2021), doi: 10.1002/jbio.202000479.
229. J.-H. Choi, S. Shin, Y. Moon, J. H. Han, E. Hwang, S. Jeong, *Spectrochim. Acta B, At. Spectrosc.* **179** (2021).
230. J. P. M. Almeida, A. L. Chen, A. Foster, R. Drezek, *Nanomedicine* **6**, 815–835 (2011).
231. L. Sancey, V. Motto-Ros, S. Kotb, X. Wang, F. Lux, G. Panczer, J. Yu, O. Tillement, *J. Vis. Exp.* (2014), doi: 10.3791/51353.
232. V. Motto-Ros, L. Sancey, X. C. Wang, Q. L. Ma, F. Lux, X. S. Bai, G. Panczer, O. Tillement, J. Yu, *Spectrochim. Acta B, At. Spectrosc.* **87**, 168–174 (2013).
233. Y. Moon, J. H. Han, J.-H. Choi, S. Shin, Y.-C. Kim, S. Jeong, *J. Biomed. Opt.* **24**, 1 (2018).
234. X. Chen, X. Li, S. Yang, X. Yu, A. Liu, *Biomed. Opt. Express* **9**, 1057–1068 (2018).
235. Y. Chu, F. Chen, Z. Sheng, D. Zhang, S. Zhang, W. Wang, H. Jin, J. Qi, L. Guo, *Biomed. Opt. Express* **11**, 4191–4202 (2020).
236. J. Wang, L. Li, P. Yang, Y. Chen, Y. Zhu, M. Tong, Z. Hao, X. Li, *Lasers Med. Sci.* **33**, 1381–1386 (2018).
237. Y. Ding, Q. Pan, W. Gao, Y. Pu, K. Luo, B. He, *Biomater. Sci.* **11**, 1182–1214 (2023).
238. Q. Shi, Y. Tong, Y. Zheng, Y. Liu, T. Yin, *Int. J. Pharm.* **633** (2023).
239. Y. Wu, Y. Li, G. Lv, W. Bu, *Chem. Sci.* **13**, 2202–2217 (2022).
240. Z. Gu, C. Yu, *J. Nanobiotechnol.* **20**, 528 (2022).
241. J. Ming, T. Zhu, W. Yang, Y. Shi, D. Huang, J. Li, S. Xiang, J. Wang, X. Chen, N. Zheng, *ACS Appl. Mater. Interfaces* **12**, 51249–51262 (2020).
242. Q. Yu, J. Zhou, J. Song, H. Zhou, B. Kang, H.-Y. Chen, J.-J. Xu, *Small* **19**, 2206592 (2023).
243. Y. Guo, H.-R. Jia, X. Zhang, X. Zhang, Q. Sun, S.-Z. Wang, J. Zhao, F.-G. Wu, *Small* **16**, 2000897 (2020).
244. S. Khattak, N. Gupta, X. Zhou, L. Pires, B. C. Wilson, Y. H. Yucel, *Exp. Eye Res.* **179**, 157–167 (2019).
245. Y. Wen, V. X. Truong, M. Li, *Nano Lett.* **21**, 3066–3074 (2021).
246. T. Hollon, D. A. Orringer, *J. Neuro-Oncol.* **151**, 393–402 (2021).